Topological monomodes in non-Hermitian systems

E. Slootman,[1, 2, *] W. Cherifi,[3, *] L. Eek,[1] R. Arouca,[4] E. J. Bergholtz,[3] M. Bourennane,[3, †] and C. Morais Smith[1]

[1]Institute for Theoretical Physics, Utrecht University, Princetonplein 5, 3584CC Utrecht, The Netherlands

[2]Adaptive Quantum Optics (AQO), MESA$^+$ Institute for Nanotechnology, University of Twente, PO Box 217, 7500 AE Enschede, The Netherlands

[3]Department of Physics, Stockholm University, S-10691, Stockholm, Sweden

[4]Department of Physics and Astronomy, Uppsala University, Uppsala, Sweden

(Dated: June 21, 2023)

Topological monomodes have been for long as elusive as magnetic monopoles. The latter was experimentally shown to emerge in effective descriptions of condensed-matter systems, while the experimental exploration of the former has largely been hindered by the complexity of the conceived setups. Here, we present a remarkably simple model and the experimental observation of topological monomodes generated *dynamically*. By focusing on non-Hermitian one-dimensional (1D) and 2D Su-Schrieffer-Heeger (SSH) models, we theoretically unveil the minimal configuration to realize a topological monomode upon engineering losses and breaking of lattice symmetries. Furthermore, we classify the systems in terms of the (non-Hermitian) symmetries that are present and calculate the corresponding topological invariants. To corroborate the theory, we present experiments in photonic lattices, in which a monomode is observed in the non-Hermitian 1D and 2D SSH models, thus breaking the paradigm that topological corner states should appear in pairs. Our findings might have profound implications for photonics and quantum optics because topological monomodes increase the robustness of corner states by preventing recombination.

* Authors contributed equally

† Corresponding author: boure@fysik.su.se

Ever since the first observation of topological behaviour through the quantum Hall effect, topological states of matter have allowed for an entirely new perspective on condensed-matter physics[1–3]. These states challenge the Ginzburg-Landau classification of phases of matter in terms of spontaneous symmetry breaking, being instead characterized by an underlying topology. The topological robustness of these materials is manifest in both the presence of topological invariants at their bulk and topologically protected states at their boundaries. Because of their dissipationless nature, topological boundary modes are expected to become a key ingredient in nanotechnology. Moreover, the zero-energy topological corner states that may appear at the edges of 1D and 2D systems are promising candidates to realize qubits in the field of quantum computing and spintronics[4–6]. For special classes of these materials, the corner states are related by symmetry, which makes them come in *pairs*. A paradigmatic example is the Su-Schrieffer-Heeger (SSH) model[7], which exhibits two edge states related by sublattice and inversion symmetry. Because these two modes are connected by symmetry and located at different ends of the lattice, they are jointly protected against symmetry-preserving perturbations. The same argument also applies to higher-order topology, where multiple symmetry-related boundary modes appear at corners (2D) or hinges (3D)[8]. An intriguing unanswered question is whether these topological pairs could be broken, and a monomode located at one single edge would still be topologically stable.

Recently, the understanding of topological states was greatly enlarged by non-Hermitian Hamiltonians[9–16], in many ways. Unique non-Hermitian topological phenomena were revealed, like the non-Abelian topological properties of exceptional points [17,18], or the non-Hermitian skin effect protected by a spectral winding number[19–22]. By allowing the Hamiltonian to be non-Hermitian, one extends the different symmetry-protected phases[9,10]. Particularly interesting is to investigate how structured loss, which acts as dissipation and one could naively expect to be detrimental to topology, can actually be harnessed for robustly targeting boundary modes, as shown in Ref. [23].

Here, we explore the consequences of non-Hermitian phenomena to design and experimentally observe a *dynamically* generated *topological monomode*. Specifically, we consider how losses, which explicitly break a symmetry of the system, affect symmetry-related boundary modes, while retaining a generalized non-Hermitian symmetry constraint. We consider loss localized in one sublattice of non-Hermitian generalizations of the SSH model in 1D and 2D, and probe the effects of both, boundaries and topological defects. To corroborate our theory, we engineer structured loss in a system of coupled waveguides, see Fig. 1**.** A schematic overview of the optical waveguide writing process is shown in Fig. 1a. Fig. 1b illustrates a 2D SSH sample. Finally, Fig. 1c gives a schematic overview of the measurement setup.

The propagation across the waveguides is described by a Schrödinger-like equation[24], such that the propagation across lossy waveguides can be represented approximately by non-Hermitian Hamiltonians[25], see Methods. Even for the simple case of loss in only one waveguide, we find that some of these corner zero-modes acquire a finite imaginary part, while others remain pinned at zero energy. Due to these spectral properties, just a subset of the topological modes survives in time,

characterizing isolated *monomodes* in 1D. However, all the boundary modes are still related by symmetry, which allowed us to show that these modes are *robust* and *characterized by topological invariants*.

The *dynamical* preparation of the monomodes set our work apart from other realizations of single isolated topological modes, like the odd site SSH chain[16], defective non-Hermitian SSH boundary states[26–28], band structure monopoles[17,18], or defect states[25,29,30]. By exploring injection of light in multiple sites, we also show that this differs from previous works that showed isolated modes due to the initial state preparation[31,32]. In contrast, we present a simple and generic way to prepare the isolated boundary modes by engineering loss, while preserving the topological aspects of these states.

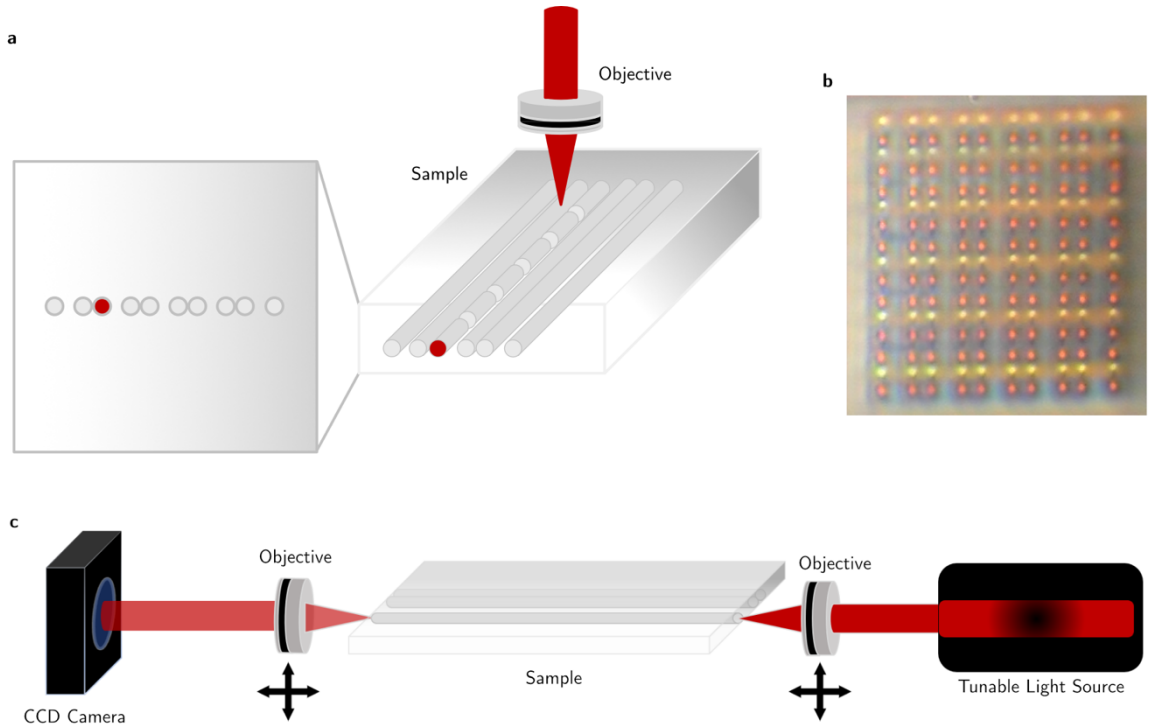

Fig. 1 | Overview of the experimental setup. a, Schematic overview of the process of creating the waveguides in the sample. The loss is introduced by making cuts in the waveguide. The light is focused using an objective. **b,** A microscopic picture of a produced 2D SSH sample. Here, $t_1 = 11$ µm and $t_2 = 7$ µm. **c,** Schematic overview of the measurement process. The light from the tunable light source is focused using an objective into a specific waveguide of the sample. At the other end, a camera captures the resulting light.

We consider a version of the SSH model, in which we introduce a loss of strength 2γ on the A sublattice[25,33–35], see Fig. 2a. This model and others with local gain and loss are discussed in more detail in the section “Gain and Loss Systems” of the Supplemental Material (SM). The Hamiltonian of this system is given by

$$H = -\sum_{n=1}^{N}\left[\left(t_1 a_n^\dagger b_n + t_2 b_n^\dagger a_{n+1} + H.c.\right) + 2i\gamma a_n^\dagger a_n\right], \qquad (1)$$

where N is the number of unit cells, and t_1, t_2 denote, respectively, the inter- and the intra-cell hopping parameter. For simplicity, we assume them to be real. The operators a_n ($a_n^\dagger$) annihilate (create) a particle in sublattice A at site n (similarly for B). The corresponding dispersion relation for periodic boundary conditions (PBC) is given by

$$\epsilon(k) = -i\gamma \pm \sqrt{-\gamma^2 + t_1^2 + t_2^2 + 2t_1 t_2 \cos(ka)}\,, \tag{2}$$

where the lattice parameter is denoted by a. We note that the spectrum of the system is similar to the one with open boundary conditions (OBC). This spectrum is also like the one of a chain with alternating gain and loss, shifted down on the imaginary axis by γ (see SM). The Hermitian SSH model ($\gamma = 0$) has a topological phase for $|t_2| > |t_1|$. In the case of OBC, this manifests itself in a pair of zero-energy edge modes. When γ is taken to be finite, one of the zero modes acquires a negative imaginary energy, while the other one remains at zero energy. This occurs because we have introduced loss only on one of the two sublattices. Each edge mode has support on one sublattice, thus exhibiting different energies. This behaviour is illustrated in Fig. 2b.

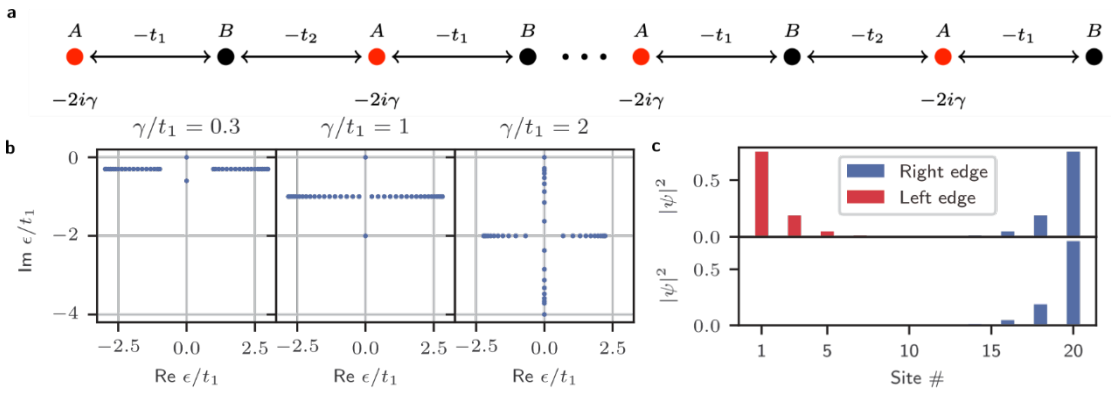

Fig. 2 | **Theoretical description of an SSH chain with loss. a,** 1D SSH lattice, described by Eq. (1). **b,** Spectrum of the SSH model with alternating loss, for OBC in the topological regime, with $t_2/t_1 = 2$. The system consists of 40 lattice sites. The energies are shown in the complex plane, for different values of γ/t_1. **c,** Time evolution of the eigenstates of the Hamiltonian given by Eq. (1). The two edge modes, for $t_2/t_1 = 2$ and $\gamma/t_1 = 2$, are depicted at $t = 0$ (top) and at $t = 10$ (bottom) for 20 lattice sites. One observes that after some time, the left edge mode has disappeared, giving rise to a monomode. The time is measured in units of $(\hbar/t_1)$.

The Hamiltonian directly encodes the information about the time-evolution of the eigenstates through

$$|\psi(t)\rangle = \mathrm{U}|\psi(0)\rangle = \mathrm{e}^{-\frac{i}{\hbar}\mathrm{H}t}|\psi(0)\rangle. \tag{3}$$

Therefore, the amplitude of states with a negative (positive) imaginary energy will decrease (increase) over time. Since only one mode of the system has a non-negative imaginary energy, see Fig. 2b, all but one of the states will decay over time. This is illustrated in Fig. 2c, where the time-evolution operator is applied to the two edge states of the system. It is clear that only the right edge mode, the one which has support on the sublattice without loss, will endure. Therefore, this system reveals

the existence of a *topological monomode.* There is a bulk invariant associated to this topological state, which takes the form of a Chern number of an effective 2D Hermitian model[36,37]. In the Methods and in the SM section "Chern Number for Alternating Loss 1D SSH", this invariant is calculated and shown to be quantized.

The monomode can nevertheless be realized in a more straightforward way. Instead of including losses in every unit cell, it is sufficient to insert loss only on a single site in the chain. The difference is that it will take longer for the bulk and the corresponding edge mode to decay. In addition, this decay time becomes size dependent. A second, more practical, constraint is that the lossy site should be 'relatively' close to the decaying edge mode, for the decay to occur more rapidly. Since the left (right) edge mode has support on the A (B) sublattice, inserting the loss on the B (A) sublattice near the left (right) edge will give the right (left) edge mode a very long lifetime. In this case, it would be difficult to observe the dynamically generated monomode. On the other hand, if we insert the loss on a site on sublattice A in the second unit cell, corresponding to the Hamiltonian

$$H = -\sum_{n=1}^{N}\left[t_1 a_n^\dagger b_n + t_2 b_n^\dagger a_{n+1} + H.c.\right] - i\gamma a_2^\dagger a_2, \qquad (4)$$

the left edge state will decay relatively fast. Nevertheless, some bulk states may take some time to decay. For a sufficiently long time, the left edge state and the bulk states belonging to the A sublattice will always decay.

This idea is not only applicable to the SSH model, but also to other models, even ones that are not in the Altland-Zirnbauer classification. We make this explicit by considering higher-order topology (HOT)[8,38,39] models. Now, we focus on the 2D SSH model, which is a HOT metal[32,40,41]. Although the 2D SSH model presents bulk states at zero energy, they do not hybridize with the robust symmetry-protected corner modes for large system sizes. We performed calculations based on the Jackiw-Rebbi method[42] and confirmed the existence of topological corner modes by detecting the change in mass profile between topological and trivial regions, see Methods and SM. The four corner modes are protected by C_{4v} and chiral symmetry, such that we can use again a similar insight to add loss in some of the sublattices and design only two or one corner state, depending on the loss distribution. See SM "Numerical Predictions" for simulations highlighting bi- and monomodes in the 2D SSH model and "Corner States of the Lossy 2D SSH model" for calculations of the loss configurations based on the Jackiw-Rebbi method.

To illustrate our findings, we now perform a set of eight experiments using waveguides for the 1D model. One experiment was realized for a simple tight-binding chain without loss, and another for a dimerized chain in the trivial limit. Both show propagation of light in the bulk. Three experiments were performed on the dimerized chain in the topological case, one without loss and two with loss. Finally, three experiments were realized with a topological defect. In this case, there is an edge mode at the end of the chain, and one at the defect. By moving the location of the loss, we show that it is possible to destroy either the edge or the defect mode.

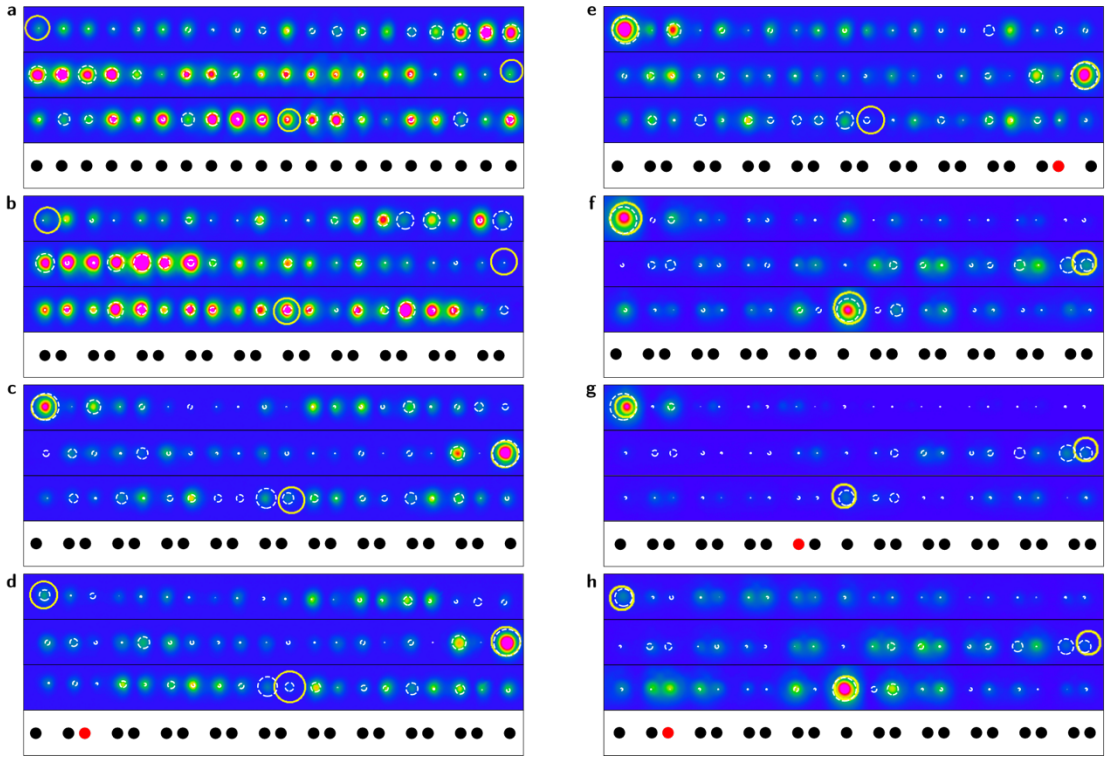

Fig. 3 | Experimental realisation of the monomode in 1D SSH chains. Yellow circles signal the point at which light was injected. The white dashed circles are the predictions of the tight-binding simulations. Their radius is proportional to the relative intensity. **a,** Tight-binding chain (black dots) with $t_1 = t_2$, dispersing into the bulk. **b,** Trivial SSH chain with $t_2/t_1 = 0.5$, dispersing into the bulk. **c,** Topological SSH chain without loss with $t_2/t_1 = 2$. Localised edge modes can be clearly observed. **d,** By adding loss ($\gamma/t_1 = 0.5$) at the red-dot site near the left edge, one of the edge modes disappears, revealing the monomode. **e,** When the loss is applied far away from the left edge, the corresponding edge mode does not decay within the experimental time scale. **f,** The inclusion of a topological defect into the system ($t_2/t_1 = 3.2$) does not affect the left edge mode, but leads to an additional mode pinned on the defect. **g,** The introduction of loss on the red-dot site near the defect destroys the mode at the defect and leads to a monomode at the edge. **h,** If instead the loss is engineered on the red-dot site near the left edge, the edge mode is destroyed, and a monomode occurs at the topological defect.

Fig. 3 shows the experimental results, along with the theoretical predictions. Yellow circles are included to indicate the point of injection of light. White, dashed, circles represent the results of the tight-binding simulations. The radius of the circles is proportional to the relative intensity. In the uniform 1D chain and in the trivial phase of the SSH model, the light disperses into the bulk (Figs. 3a and 3b, respectively). In the topological phase without loss, there are two edge modes (Fig. 3c). However, when we add loss on the A sublattice near the left edge (see red dot in Fig. 3d), we only observe one edge mode on the right-hand side (B sublattice). When the loss is placed on the A sublattice but far away from the left edge (Fig. 3e), the left edge mode does not feel it immediately, and does not decay within the time scale of the experiment. This is in agreement with the theoretical predictions, represented by the white dashed circles (see the SM section “Numerical Predictions” for a stand-alone figure of the theoretical predictions). When the system hosts a topological defect in

the centre of the chain, there is an edge mode on the left edge of the chain, as well as a mode pinned on the defect (Fig. 3f). By putting loss on the B sublattice near the defect, the mode pinned on the defect can be destroyed, while leaving the left edge mode intact (Fig. 3g). Similarly, the loss can be placed on the A sublattice near the left edge, thus removing the edge mode, but leaving the monomode on the defect (Fig. 3h). The existence of the topological mode at a defect is also understood in the framework of Jackiw-Rebbi theory[42], which is further elaborated upon in the Methods and in the SM section “Topological Defect”.

For the 2D model, three experiments were realised. The first experiment shows the existence of four corner modes. By placing loss on two sublattices, the C_{4v} symmetry is reduced to C_{2v}, and the amount of corner modes is reduced to two, yielding bimodes. By adding more loss and breaking the C_{2v} symmetry further, the bimodes can be reduced to a single corner, thus revealing a monomode.

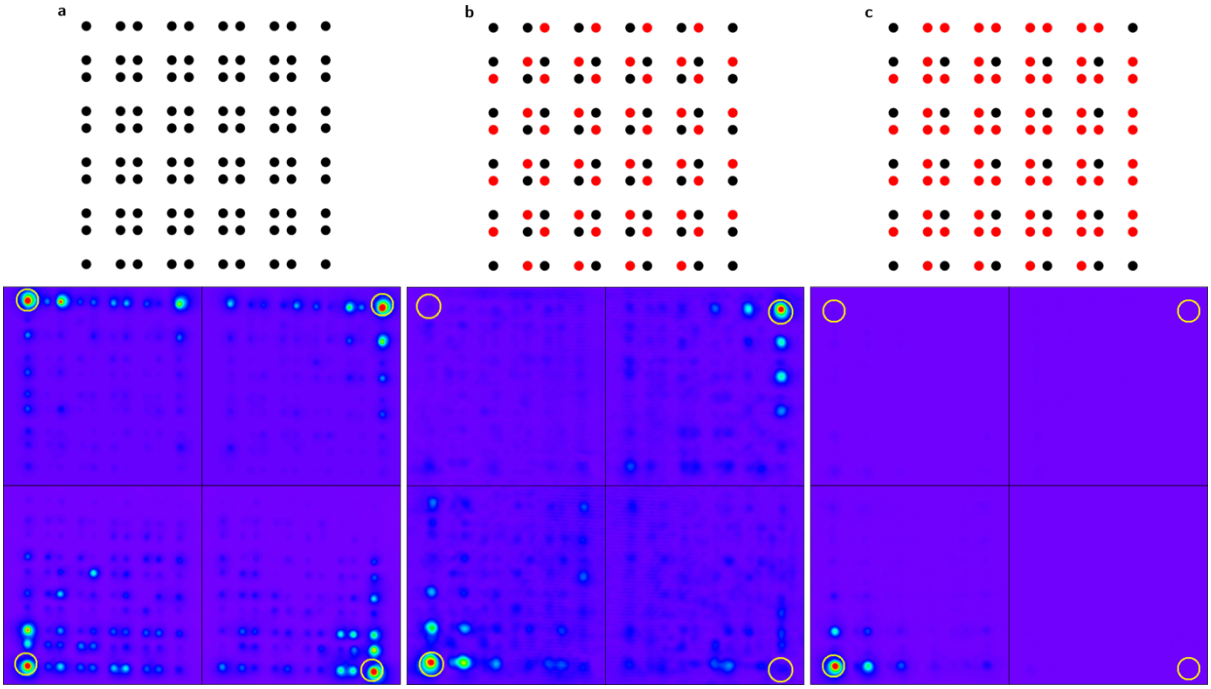

Fig. 4 | Experimental realisation of bi- and monomodes in the 2D SSH model. Yellow circles signal the point at which light was injected. For numerical predictions, see the SM “Numerical Predictions”. Top row shows the loss locations in the lattice (red dots) and the bottom row the experiments. Each quarter of the bottom images is one experimental realization, with light injected into the indicated corner (yellow circles). **a,** In the absence of loss, there are four distinct corner modes. **b,** Loss is implemented on two sublattices. This breaks the C_{4v} symmetry of the system into C_{2v} and leads to bimodes. **c,** By adding loss on three sublattices, the C_{2v} symmetry is broken and the monomode emerges.

Fig. 4 shows the results of the experiment for the 2D model. Yellow circles are included to signal the point of injection of light. In the lossless case, the system hosts four corner modes (Fig. 4a). By adding loss to two sublattices, two of the corresponding corner modes are destroyed, leaving bimodes (Fig. 4b). Adding loss to one more sublattice reveals a monomode in the 2D SSH model (Fig. 4c). This is in full agreement with the theoretical predictions (see SM “Numerical Predictions”).

We have theoretically and experimentally shown the existence of topological monomodes in non-Hermitian systems through the engineering of loss. By introducing losses on a selected sublattice and sufficiently close to the corresponding edge, one of the topological edge modes will decay over time. We have realised these monomodes experimentally in a photonic lattice. Moreover, we confirmed the robustness of the monomodes against perturbations. It is remarkable that a generalised topological invariant protecting the corner mode remains valid in this non-Hermitian setup. The implications of our results are multifold. On the one hand, we have identified an extremely simple model, capable of revealing monomodes. Since those cannot recombine with their corresponding partner, those monomodes would be ideal candidates for transmitting information based on topological states. Here, we have the additional advantage that this mode will not hybridize, and hence exhibits further robustness with respect to its Hermitian counterpart. In this context, it is important to note that the phenomena explored in this work generalizes, *mutatis mutandis,* to quantum master equations[43,44]. A natural extension of this work is to explore the presence of such states in other Z_2 topological classes and investigate whether engineered loss in another inner degrees of freedom (like spin or particle/hole) can also be used to generate monomodes.

Acknowledgement

The authors thank J.C. Budich, J. Carlström, T. Nag, A. Black-Schaffer, and J.A. Klärs for useful discussions. WC, RA, EJB, and MB thank the Knut and Alice Wallenberg Foundation for financial support (grant numbers 31002636, 2018.0071, and 31001206). WC, EJB, and MB thank the Swedish Research Council for financial support (grant numbers 2017-04855 and 31001205). LE and CMS acknowledge the research program “Materials for the Quantum Age” (QuMat) for financial support. This program (registration number 024.005.006) is part of the Gravitation program financed by the Dutch Ministry of Education, Culture and Science (OCW).

Author contribution

ES did almost all theoretical calculations under the supervision of LE, RA, and CMS. The Chern numbers were calculated by LE, and the topology in the framework of the Jackiw-Rebbi theory was calculated by RA under the supervision of EJB. The experiments were performed by WC under the supervision of MB. CMS coordinated the entire project. All authors discussed the results and contributed to the elaboration of the manuscript.

Methods

Theoretical Methods

The time-evolution of the systems described by the Eqs. (1) and (4) was calculated by writing the Hamiltonians in matrix form and obtaining the eigenvectors and eigenvalues numerically. The resulting Hamiltonian in matrix form is given by

$$H = \boldsymbol{c}^{\dagger} \begin{pmatrix} -2\gamma i & -t_1 & 0 & \cdots & 0 \\ -t_1 & 0 & -t_2 & & \\ 0 & -t_2 & -2\gamma i & & \vdots \\ \vdots & & & \ddots & \\ 0 & & \cdots & & 0 \end{pmatrix} \boldsymbol{c} \tag{5}$$

for Eq. (1) and by

$$H = \boldsymbol{c}^{\dagger} \begin{pmatrix} 0 & -t_1 & 0 & \cdots & 0 \\ -t_1 & 0 & -t_2 & & \\ 0 & -t_2 & -\gamma i & & \vdots \\ \vdots & & & \ddots & \\ 0 & & \cdots & & 0 \end{pmatrix} \boldsymbol{c} \tag{6}$$

for Eq. (4). In Eq. (6), the remaining terms along the diagonal are zero. Here, $\boldsymbol{c}^{\dagger}$and $\boldsymbol{c}$ are the creation and annihilation operators, respectively. The eigenvectors are evolved in time by letting Eq. (3) operate on the eigenvectors.

Topological Characterization

Even though sublattice symmetry is broken by the presence of on-site loss, (non-Hermitian) chiral symmetry Γ: $\Gamma \mathrm{H} \Gamma = -\mathrm{H}^{\dagger}$ is still present for alternating loss. As a result, it is possible to characterize the phases of the non-Hermitian SSH model in terms of a topological invariant. The calculation of this invariant is based on defining a 2D ancestor Hamiltonian, for which a Chern number can be calculated. Following the framework introduced in Refs. [36,37], we obtain the following effective Hermitian Hamiltonian:

$$H^{\mathrm{eff}}(k, \eta) = \Gamma\big(\eta \mathbb{I} - i H_{NH-SSH}(k)\big) \quad \text{with} \quad \Gamma = \sigma_z. \tag{7}$$

From this, we can calculate the Berry curvature as a function of k and η, (see section "Chern number for alternating loss 1D SSH" of the SM), which yields the Chern number

$$C = \begin{cases} 0 & |t_1| > |t_2| \\ 1 & |t_1| < |t_2| \end{cases}. \tag{8}$$

We remark that this bulk invariant was computed for the system with alternating loss, since it is a translation invariant version of the model with a single lossy site, with the same topological properties, since it belongs to the same symmetry class.

The methodology of the effective Hamiltonian from Refs. [36,37] is also used to investigate both the topological defect and the corner modes of the 2D SSH mode (see sections "Effective Hamiltonian for the 2D SSH", "Topological defect", and "Corner states of the lossy 2D SSH model" of the SM). For this, we use the Jackiw-Rebbi construction,[38,42] which consists in analysing a low-energy Hamiltonian close to the gap point and use different mass profiles to account for the boundary between topological and trivial phases.

For the topological defect (section “Topological defect” of the SM), we obtain the continuum Hamiltonian

$$H^{\text{eff}}(x,\eta) = \left(\eta - \frac{\gamma}{2}\right)\sigma_z + t_2(x)\, M(x)\sigma_y + i t_2(x)\, \partial_x \sigma_x, \tag{9}$$

where we introduced the mass term $M(x) = [t_1(x) - t_2(x)]/t_2(x)$. The mass term characterizes the topological phase, being negative (positive) for the topological (trivial) phase. A topological defect may be viewed as a domain boundary between both phases. This behaviour is captured by letting the mass term be spatially dependent, such that $M(x)$ changes sign across a topological defect, implying a localized solution.

The same method can be used to show the topological characteristic of the corner modes in the 2D SSH model. Even though this model does not present a gapped bulk spectrum, zero energy modes localized in the corner only appear at the HOT phase. We start by extending the method from Refs. [36,37] to non-Hermitian 2D systems. For the 2D SSH model, it takes the form (section “Effective Hamiltonian for the 2D SSH” of the SM)

$$H^{\text{eff}}(\boldsymbol{k},\eta) = \Gamma\left(\eta\, \mathbb{I} \otimes \mathbb{I} - i H_{NH-2D-SSH}(\boldsymbol{k})\right) \quad \text{where} \quad \Gamma \equiv \sigma_z \otimes \mathbb{I}. \tag{10}$$

Although there is no longer a Chern number associated with this model, it is still useful to analyse the topological properties of boundary states (section “Corner states of the lossy 2D SSH model” of the SM). We obtain the low-energy Hamiltonian

$$H^{\text{eff}}(\boldsymbol{p},\eta) = H_d(\eta) + t_2 M^x \sigma_y \otimes \mathbb{I} - t_2 p_x \sigma_x \otimes \sigma_z + t_2 M^y \sigma_y \otimes \sigma_x + t_2 p_y \sigma_y \otimes \sigma_y, \tag{11}$$

with $p_x = k_x - \pi$ and $p_y = k_y - \pi$. Again, the topological phase is characterized by the mass terms $M^{x/y}$. To model the different boundaries, we set t_1 to be different across x and y and define $M^{x/y} = \left(t_1^{x/y} - t_2\right)/t_2$. The HOT phase is marked by negative M^x and M^y, while we model the exterior of the lattice by a trivial insulator with positive $M^{x/y}$. We show that one obtains localized states at the corners only when there is this change of sign for the mass term, indicating the topological aspect of these zero-energy boundary modes.

Experimental Methods

To experimentally validate the existence of monomodes, a photonic waveguide lattice was built. Although the theoretical model is quantum, it can be experimentally simulated using classical light. Details of the experiment are described in the section “Experimental details” of the SM. In this experimental setup, the propagation of the light is determined by the paraxial equation[24]

$$i\frac{\partial}{\partial z}\Psi(x,y,z) = \left[-\frac{1}{2k_0}\left(\frac{\partial^2}{\partial x^2} + \frac{\partial^2}{\partial y^2}\right) - \frac{k_0 \Delta n(x,y)}{n_0}\right]\Psi(x,y,z) \tag{12}$$

Here, Ψ acts as the wavefunction for the electric field, $k_0 = n_0\omega/c$, with ω the light frequency, and n_0 the refractive index. Δn is the change in refractive index. The paraxial equation has a structure similar to the Schrödinger equation. This system can be used to model the tight-binding Hamiltonian, where the hopping terms depend on the distance d_i between the waveguides, $t_i \approx e^{-d_i/\xi}$. ξ depends on the parameters of the experiment, such as the wavelength of the light.

We achieve the desired loss in the system by introducing a certain concentration of microscopic scattering points along the waveguides through the dwelling process. The direct laser-writing technology provided us with the ability to freely tune both the dwelling time and the separation between the individual scattering points, allowing for the implementation of a wide range of artificial losses. Importantly, this process neither compromises the real part of the refractive index nor introduces directionality into the system.

The direct laser-writing technique offered us precise control over the amount and distribution of loss in the waveguide lattice, enabling us to design and fabricate the lattice with the desired characteristics. For the 1D experiment, the distance between the waveguides was set to $d_1 = 12$ μm and $d_2 = 10$ μm for the first five experiments. This yields a ratio of $t_2/t_1 \approx 2$ for the topological case. In the topological defect experiments, the distances of $d_1 = 11$ μm and $d_2 = 7$ μm were used, giving a ratio of $t_2/t_1 \approx 3.2$. The loss for the first five experiments was engineered by making scattering points 0.2 mm apart in the waveguide, by waiting 0.5 s with the laser. For the last three (topological defect) experiments, the loss was engineered by adding 50 cuts of 350 μm along the waveguide. To ensure that the edge states would not hybridise before the measurement, a system size of 10 unit cells was chosen. For the 2D experiments, the distance between the waveguides was set to $d_1 = 11$ μm and $d_2 = 7$ μm. This yields a ratio of $t_2/t_1 \approx 3.2$. The loss was engineered by adding 100 cuts of 70 μm along the waveguide. A system of 5 by 5 unit cells was used.

References

1. Hasan, M. Z. & Kane, C. L. Colloquium : Topological insulators. *Rev. Mod. Phys.* **82**, 3045–3067 (2010).
2. Bernevig, B. A. & Hughes, T. L. *Topological insulators and topological superconductors*. (Princeton University Press, 2013).
3. Qi, X.-L. & Zhang, S.-C. Topological insulators and superconductors. *Rev. Mod. Phys.* **83**, 1057–1110 (2011).
4. Pesin, D. & MacDonald, A. H. Spintronics and pseudospintronics in graphene and topological insulators. *Nat. Mater.* **11**, 409–416 (2012).
5. Sarma, S. D., Freedman, M. & Nayak, C. Majorana zero modes and topological quantum computation. *NPJ Quantum Inf.* **1**, 15001 (2015).
6. He, M., Sun, H. & He, Q. L. Topological insulator: Spintronics and quantum computations. *Front. Phys.* **14**, 43401 (2019).
7. Su, W. P., Schrieffer, J. R. & Heeger, A. J. Solitons in Polyacetylene. *Phys. Rev. Lett.* **42**, 1698 (1979).
8. Benalcazar, W. A., Bernevig, B. A. & Hughes, T. L. Quantized electric multipole insulators. *Science* **357**, 61–66 (2017).

9. Gong, Z. *et al.* Topological phases of non-Hermitian systems. *Phys. Rev. X* **8**, 031079 (2018).
10. Kawabata, K., Shiozaki, K., Ueda, M. & Sato, M. Symmetry and Topology in Non-Hermitian Physics. *Phys. Rev. X* **9**, 041015 (2019).
11. Bergholtz, E. J., Budich, J. C. & Kunst, F. K. Exceptional topology of non-Hermitian systems. *Rev. Mod. Phys.* **93**, 015005 (2021).
12. Zeuner, J. M. *et al.* Observation of a topological transition in the bulk of a non-Hermitian system. *Phys. Rev. Lett.* **115**, 040402 (2015).
13. Pan, M., Zhao, H., Miao, P., Longhi, S. & Feng, L. Photonic zero mode in a non-Hermitian photonic lattice. *Nat. Commun.* **9**, 1308 (2018).
14. Helbig, T. *et al.* Generalized bulk–boundary correspondence in non-Hermitian topolectrical circuits. *Nat. Phys.* **16**, 747–750 (2020).
15. Xiao, L. *et al.* Non-Hermitian bulk–boundary correspondence in quantum dynamics. *Nat. Phys.* **16**, 761–766 (2020).
16. Ghatak, A., Brandenbourger, M., Van Wezel, J. & Coulais, C. Observation of non-Hermitian topology and its bulk–edge correspondence in an active mechanical metamaterial. *PNAS* **117**, 29561–29568 (2020).
17. Pap, E. J., Boer, D. & Waalkens, H. Non-Abelian nature of systems with multiple exceptional points. *Phys. Rev. A* **98**, 023818 (2018).
18. König, J. L. K., Yang, K., Budich, J. C. & Bergholtz, E. J. Braid Protected Topological Band Structures with Unpaired Exceptional Points. Preprint at http://arxiv.org/abs/2211.05788 (2022).
19. Esaki, K., Sato, M., Hasebe, K. & Kohmoto, M. Edge states and topological phases in non-Hermitian systems. *Phys. Rev. B* **84**, 205128 (2011).
20. Herviou, L., Bardarson, J. H. & Regnault, N. Defining a bulk-edge correspondence for non-Hermitian Hamiltonians via singular-value decomposition. *Phys. Rev. A* **99**, 052118 (2019).
21. Okuma, N. & Sato, M. Non-Hermitian Topological Phenomena: A Review. *Annu. Rev. Condens. Matter Phys.* **14**, 83–107 (2023).
22. Lin, R., Tai, T., Li, L. & Lee, C. H. Topological Non-Hermitian skin effect. Preprint at http://arxiv.org/abs/2302.03057 (2023).
23. Cherifi, W., Carlström, J., Bourennane, M. & Bergholtz, E. J. Non-Hermitian Boundary State Distillation with Lossy Waveguides. Preprint at http://arxiv.org/abs/2304.03016 (2023).
24. Longhi, S. Quantum-optical analogies using photonic structures. *Laser Photonics Rev.* **3**, 243–261 (2009).
25. Weimann, S. *et al.* Topologically protected bound states in photonic parity–time-symmetric crystals. *Nat. Mater.* **16**, 433–438 (2017).
26. Lee, T. E. Anomalous Edge State in a Non-Hermitian Lattice. *Phys. Rev. Lett.* **116**, 133903 (2016).
27. Kunst, F. K., Edvardsson, E., Budich, J. C. & Bergholtz, E. J. Biorthogonal Bulk-Boundary Correspondence in Non-Hermitian Systems. *Phys. Rev. Lett.* **121**, 026808 (2018).
28. Yao, S. & Wang, Z. Edge States and Topological Invariants of Non-Hermitian Systems. *Phys. Rev. Lett.* **121**, 086803 (2018).
29. Poli, C., Bellec, M., Kuhl, U., Mortessagne, F. & Schomerus, H. Selective enhancement of topologically induced interface states in a dielectric resonator chain. *Nat. Commun.* **6**, 6710 (2015).

30. Noh, J. *et al.* Topological protection of photonic mid-gap defect modes. *Nat. Photon* **12**, 408–415 (2018).
31. El Hassan, A. *et al.* Corner states of light in photonic waveguides. *Nat. Photon* **13**, 697–700 (2019).
32. Cerjan, A., Jürgensen, M., Benalcazar, W. A., Mukherjee, S. & Rechtsman, M. C. Observation of a Higher-Order Topological Bound State in the Continuum. *Phys. Rev. Lett.* **125**, 213901 (2020).
33. Dangel, F., Wagner, M., Cartarius, H., Main, J. & Wunner, G. Topological invariants in dissipative extensions of the Su-Schrieffer-Heeger model. *Phys. Rev. A* **98**, 013628 (2018).
34. Roccati, F., Palma, G. M., Ciccarello, F. & Bagarello, F. Non-Hermitian Physics and Master Equations. *OSID* **29**, 2250004 (2022).
35. Miri, M.-A. & Alù, A. Exceptional points in optics and photonics. *Science* **363**, eaar7709 (2019).
36. Brzezicki, W. & Hyart, T. Hidden Chern number in one-dimensional non-Hermitian chiral-symmetric systems. *Phys. Rev. B* **100**, 161105 (2019).
37. Hyart, T. & Lado, J. L. Non-Hermitian many-body topological excitations in interacting quantum dots. *Phys. Rev. Res.* **4**, L012006 (2022).
38. Benalcazar, W. A., Bernevig, B. A. & Hughes, T. L. Electric multipole moments, topological multipole moment pumping, and chiral hinge states in crystalline insulators. *Phys. Rev. B* **96**, 245115 (2017).
39. Schindler, F. *et al.* Higher-order topological insulators. *Sci. Adv.* **4**, eaat0346 (2018).
40. Benalcazar, W. A. & Cerjan, A. Bound states in the continuum of higher-order topological insulators. *Phys. Rev. B* **101**, 161116 (2020).
41. Cerjan, A. & Loring, T. A. Local invariants identify topology in metals and gapless systems. *Phys. Rev. B* **106**, 064109 (2022).
42. Jackiw, R. & Rebbi, C. Solitons with fermion number 1/2. *Phys. Rev. D* **13**, 3398–3409 (1976).
43. Hegde, S. S., Ehmcke, T. & Meng, T. Edge-selective extremal damping from topological heritage of dissipative Chern insulators. Preprint at https://doi.org/10.48550/arXiv.2304.09040 (2023).
44. Yang, F., Molignini, P. & Bergholtz, E. J. Dissipative Boundary State Preparation. Preprint at https://doi.org/10.48550/arXiv.2305.00031 (2023).

Supplemental material for 'Topological Monomodes in non-Hermitian Systems'

E. Slootman,[1,2,*] W. Cherifi,[3,*] L. Eek,[1] R. Arouca,[4] E. J. Bergholtz,[3] M. Bourennane,[3,†] and C. Morais Smith[1]

[1] *Institute for Theoretical Physics, Utrecht University, Princetonplein 5, 3584CC Utrecht, The Netherlands*
[2] *Adaptive Quantum Optics (AQO), MESA+ Institute for Nanotechnology, University of Twente, PO Box 217, 7500 AE Enschede, The Netherlands*
[3] *Department of Physics, Stockholm University, S-10691, Stockholm, Sweden*
[4] *Department of Physics and Astronomy, Uppsala University, Uppsala, Sweden*

(Dated: June 21, 2023)

I. GAIN AND LOSS SYSTEMS

Here, we investigate different loss configurations in the SSH model. In this case, the non-Hermiticty will be caused by gain and/or loss on the sites. We will start by looking at the dimer with both gain and loss, followed by the SSH model with gain and loss. Henceforth, we will study a system with only loss.

A. Broken $\mathcal{PT}$-symmetry

The systems discussed here can exhibit $\mathcal{PT}$-symmetry, depending on the system size and choice of parameters. $\mathcal{PT}$-symmetry is the invariance of a system to combined parity ($x \to -x$) and time inversion ($t \to -t$) transformations. To illustrate how this works, we will discuss a very small and simple system showing both a $\mathcal{PT}$-conserved phase and a spontaneously broken phase. We note that the same reasoning works for larger lattices. The system consists of two sites, with gain $i\gamma$, loss $-i\gamma$, and hopping t_1 between the sites. The Hamiltonian reads

$$H = \mathbf{c}^\dagger \begin{pmatrix} -i\gamma & -t_1 \\ -t_1 & i\gamma \end{pmatrix} \mathbf{c}, \tag{S1}$$

where $\mathbf{c}$ ($\mathbf{c}^\dagger$) are vectors of annihilation (creation) operators. The Hamiltonian of Eq. (S1) is clearly non-Hermitian and $\mathcal{PT}$-symmetric. Its eigenvectors and eigenvalues are given by

$$\phi_\pm = \begin{pmatrix} -\frac{-i\gamma \pm \sqrt{t_1^2 - \gamma^2}}{t_1} \\ 1 \end{pmatrix} \quad \text{and} \quad \epsilon_\pm = \pm\sqrt{t_1^2 - \gamma^2}. \tag{S2}$$

There is an exceptional point at $\gamma = t_1$ because at this point both eigenvalues are 0 and both eigenvectors are $\phi = \begin{pmatrix} i & 1 \end{pmatrix}^T$. For $\gamma < t_1$, the spectrum has fully real eigenvalues, but for $\gamma > t_1$ it has fully imaginary eigenvalues, in conjugated pairs. This suggests the $\mathcal{PT}$-symmetry is broken for $\gamma > t_1$, which can be proven considering the eigenvectors of the system. For $\gamma < t_1$, we have

$$\mathcal{PT}\phi_\pm = \mathcal{P}\begin{pmatrix} -\frac{i\gamma \pm \sqrt{t_1^2 - \gamma^2}}{t_1} \\ 1 \end{pmatrix} = \begin{pmatrix} 1 \\ -\frac{i\gamma \pm \sqrt{t_1^2 - \gamma^2}}{t_1} \end{pmatrix}. \tag{S3}$$

Now, we multiply the resulting vector by a constant to obtain

$$\mathcal{PT}\phi_\pm = \begin{pmatrix} -\frac{t_1}{i\gamma \pm \sqrt{t_1^2 - \gamma^2}} \\ 1 \end{pmatrix} = \begin{pmatrix} -\frac{-i\gamma \pm \sqrt{t_1^2 - \gamma^2}}{t_1} \\ 1 \end{pmatrix} = \phi_\pm, \tag{S4}$$

so the eigenvectors are indeed $\mathcal{PT}$-symmetric. When $\gamma > t_1$, the eigenvectors are equal to

$$\phi_\pm = \begin{pmatrix} -\frac{-i\gamma \pm i\sqrt{\gamma^2 - t_1^2}}{t_1} \\ 1 \end{pmatrix} \tag{S5}$$

* Authors contributed equally
† Corresponding author: boure@fysik.su.se

and when we now apply the $\mathcal{PT}$ operators to it, we obtain

$$\mathcal{PT}\begin{pmatrix} -\frac{-i\gamma\pm i\sqrt{\gamma^2-t_1^2}}{t_1} \\ 1 \end{pmatrix} = \mathcal{P}\begin{pmatrix} -\frac{i\gamma\mp i\sqrt{\gamma^2-t_1^2}}{t_1} \\ 1 \end{pmatrix} = \begin{pmatrix} 1 \\ -\frac{i\gamma\mp i\sqrt{\gamma^2-t_1^2}}{t_1} \end{pmatrix} \rightarrow \mathcal{PT}\phi_\pm = \begin{pmatrix} -\frac{t_1}{i\gamma\mp i\sqrt{\gamma^2-t_1^2}} \\ 1 \end{pmatrix} \neq \phi_\pm. \tag{S6}$$

We indeed find that the eigenvectors are no longer $\mathcal{PT}$-symmetric if $\gamma > t_1$ and thus, the eigenvalues become complex. However, when the system size increases, this $\mathcal{PT}$-symmetric region decreases in size, such that the $\mathcal{PT}$-symmetric phase is absent in the thermodynamic limit.

B. Alternating Gain and Loss

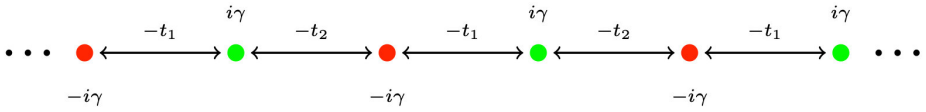

FIG. S1. SSH chain with alternating gain and loss.

We now consider a reciprocal SSH chain with alternating gain and loss on the sites [S1, S2], a system that has been extensively discussed in the literature, see Fig. S1. The reason why these imaginary contributions on the site lead to gain or loss can be understood straightforwardly by looking at the time propagator,

$$U(t) = e^{-\frac{i}{\hbar}\hat{H}t}, \tag{S7}$$

where t is time. By acting with this operator on an eigenstate of H, $|\psi_n\rangle$, the state will evolve in time according to its eigenvalue

$$U(t)\,|\psi\rangle = e^{-\frac{i}{\hbar}\epsilon_n t}\,|\psi_n\rangle\,. \tag{S8}$$

When there are losses at the sites, the eigenvalues acquire a negative imaginary contribution. This will cause an exponential decay of the state, meaning loss. In the same way, positive imaginary contributions to the eigenvalues signify gain. The matrix Hamiltonian of this system is given by

$$H = \mathbf{c}^\dagger \begin{pmatrix} -\gamma i & -t_1 & 0 & \cdots & b \\ -t_1 & \gamma i & -t_2 & & \\ 0 & -t_2 & -\gamma i & & \vdots \\ \vdots & & & \ddots & \\ b & & \cdots & & \gamma i \end{pmatrix} \mathbf{c}, \tag{S9}$$

where b is $-t_2$ or zero for periodic (PBC) or open boundary conditions (OBC), respectively. After diagonalizing the matrix we get,

$$\epsilon(k) = \pm\sqrt{-\gamma^2 + t_1^2 + t_2^2 + 2t_1 t_2\cos(ka)}. \tag{S10}$$

We can now study this system in the topological and trivial regime.

1. *Trivial Phase*

In the trivial regime of the SSH model, $|t_1/t_2| \leq 1$, the system has a fully real spectrum for $|\gamma| \leq |t_1 - t_2|$ because the eigenvectors of the Hamiltonian remain $\mathcal{PT}$-symmetric. This can be seen in Figs. S2a-b, where the imaginary part is zero for $|\gamma| < |t_1 - t_2|$ ($|t_1 - t_2| = 0.5$ as $t_1 = 1$ and $t_2 = 0.5$). In this regime, the system also has a (real) band gap. The system opens up a line gap for $|\gamma| > |t_1 + t_2|$. A line gap is present when one can draw a line between two segments of the spectrum. This is different to a point gap, where the spectrum is encircling a point. Different representations of the spectrum can be seen in Figs. S2a-c. In the case of OBC, the spectra of the system will not change much besides finite-size effects, being equal to the PBC one in the thermodynamic limit.

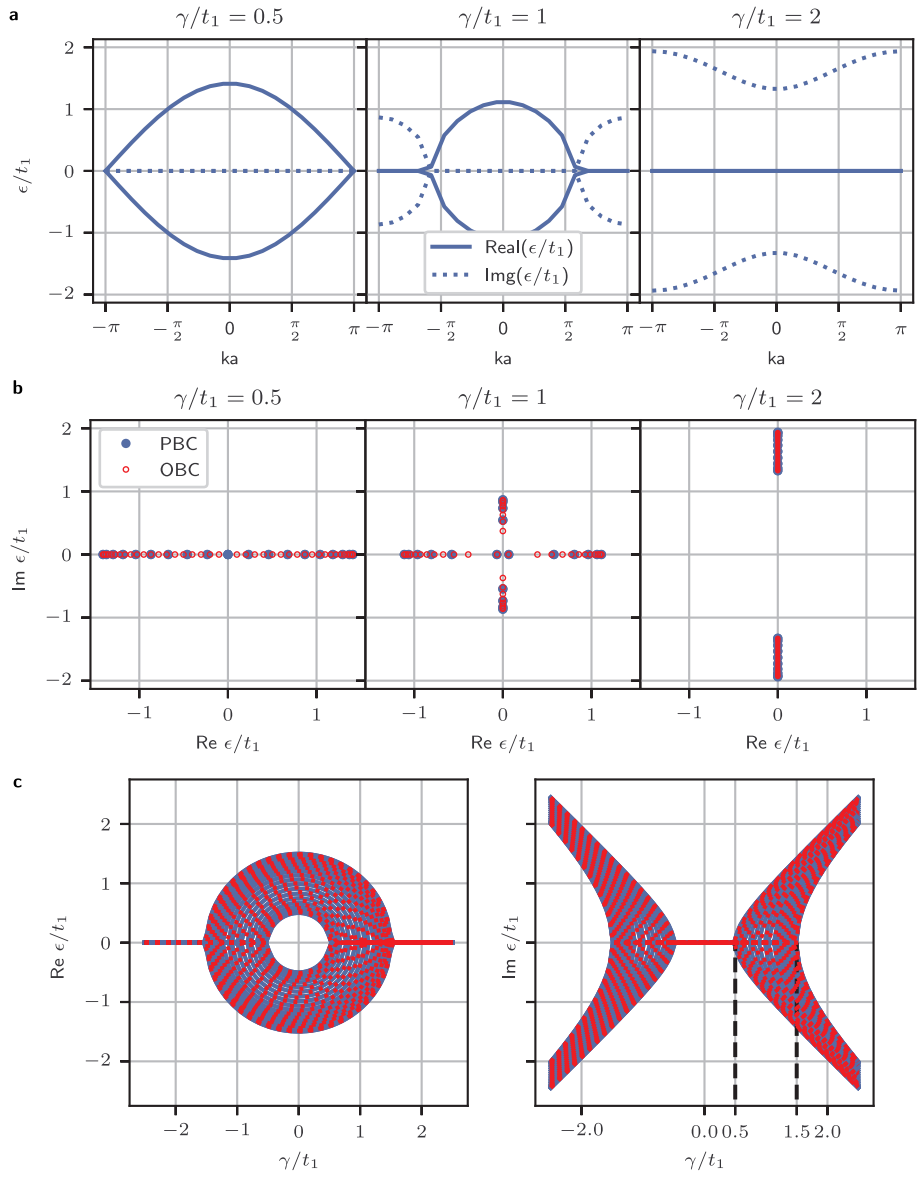

FIG. S2. Spectrum of the SSH model with alternating gain and loss for PBC and OBC in the trivial regime $t_2 = t_1/2$. A system size of 20 unit cells was used. **a**, As a function of ka for different values of γ. **b**, In the complex plane for different values of γ. The blue full circles results correspond to PBC, and the red empty circles to OBC. **c**, As a function of γ/t_1.

2. *Topological Phase*

The topological regime of the SSH model exists when $|t_2/t_1| > 1$. In this section, we will specifically consider the case when $t_2 = 2t_1$. For PBC, the system behaves in the same way as in the trivial regime. $\mathcal{PT}$-symmetry is conserved for $|\gamma| \leq |t_1 - t_2|$ and the system opens up a line gap for $|\gamma| > |t_1 + t_2|$. Different representations of the spectrum can be seen in Figs. S3a-c. The topological regime of the SSH model is more interesting in the OBC case, in which there are topologically-protected midgap states. In this non-Hermitian SSH model, these edge modes will no longer have zero energy. In Fig. S3b, the spectra in the imaginary plane is given for specific parameters. The zero energy modes have each acquired an imaginary energy. One mode acquired $+i\gamma$, while the other got $-i\gamma$. These zero modes are also clearly visible in Fig. S3c, where they are the cause of the $\mathcal{PT}$-symmetry breaking for all values $|\gamma| > 0$.

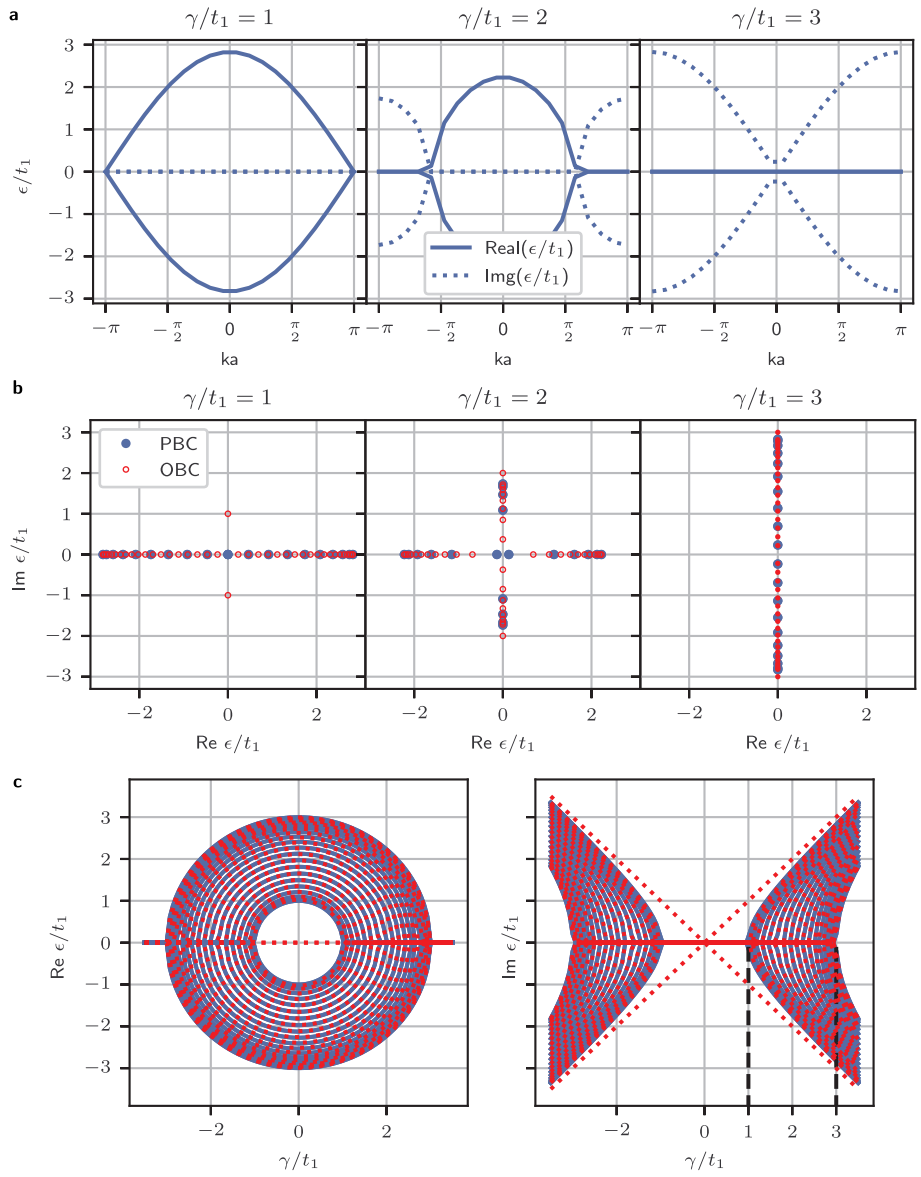

FIG. S3. Spectrum of the SSH model with alternating gain and loss for PBC and OBC in the topological regime $t_2 = 2t_1$. A system size of 20 unit cells was used. **a**, As a function of ka for different values of γ. **b**, In the complex plane for different values of γ. The blue line results correspond to PBC, and the red line to OBC. **c**, As a function of γ/t_1.

C. Alternating Loss

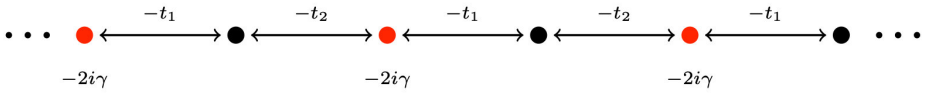

FIG. S4. SSH chain with alternating loss.

Up until this point, we have been considering systems with gain as well as loss. In an experimental setting, gain would be more difficult to engineer than loss. In order to adapt the theory to this, we can transform the system of

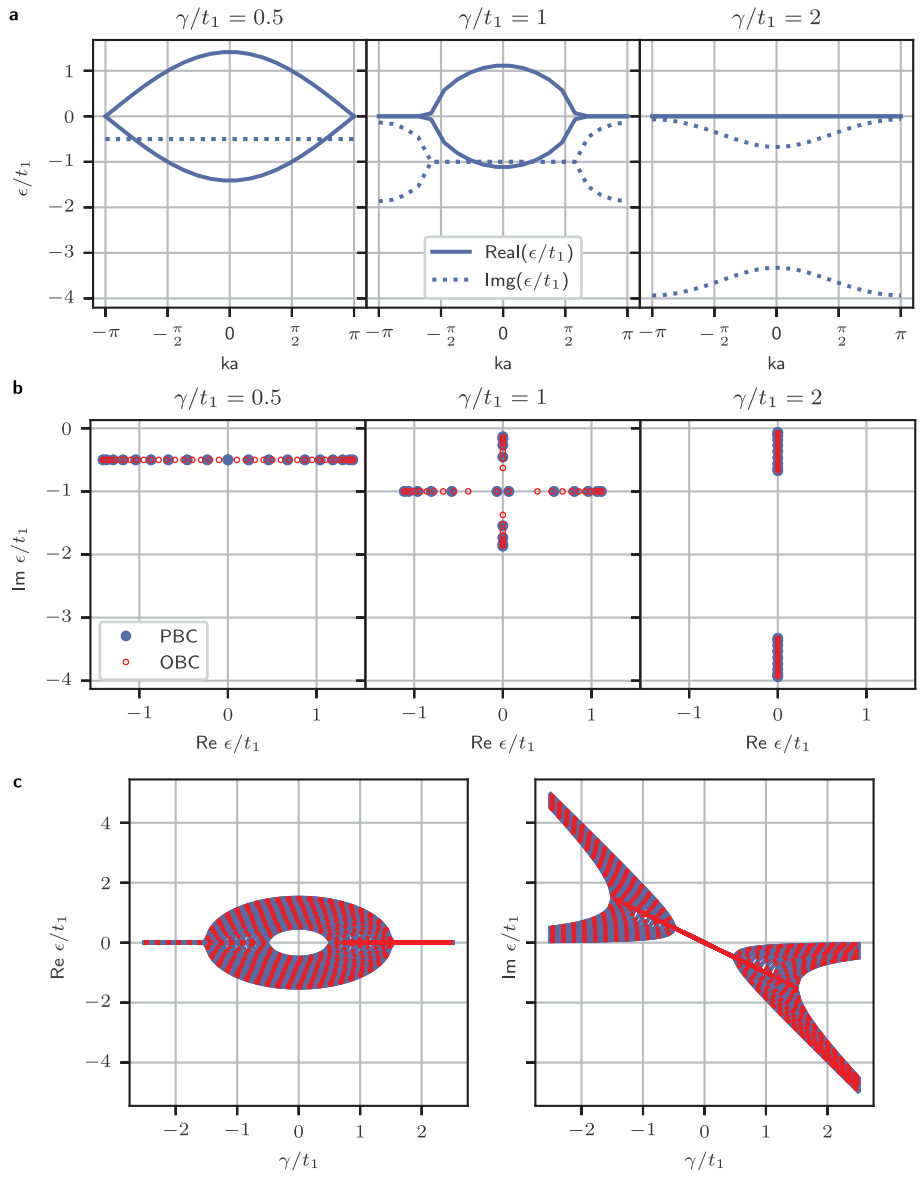

FIG. S5. Spectrum of the SSH model with alternating loss for PBC and OBC in the trivial regime $t_2 = t_1/2$. A system size of 20 unit cells was used. **a**, As a function of ka for different values of γ. **b**, In the complex plane for different values of γ. The blue full circles results correspond to PBC, and the red empty circles to OBC. **c**, As a function of γ/t_1.

Eq. (S9) to a system with only loss, by simply subtracting $i\gamma\mathbb{1}$ from it. This results in

$$H = \mathbf{c}^\dagger \begin{pmatrix} -2\gamma i & -t_1 & 0 & \cdots & b \\ -t_1 & 0 & -t_2 & & \\ 0 & -t_2 & -2\gamma i & & \vdots \\ \vdots & & & \ddots & \\ b & & \cdots & & 0 \end{pmatrix} \mathbf{c}, \tag{S11}$$

where b is $-t_2$ (0) for PBC (OBC). This results in a spectrum very similar to the spectrum of Eq. (S10), except that it has an imaginary offset

$$\epsilon(k) = \pm\sqrt{-\gamma^2 + t_1^2 + t_2^2 + 2t_1 t_2 \cos(ka)} - i\gamma. \tag{S12}$$

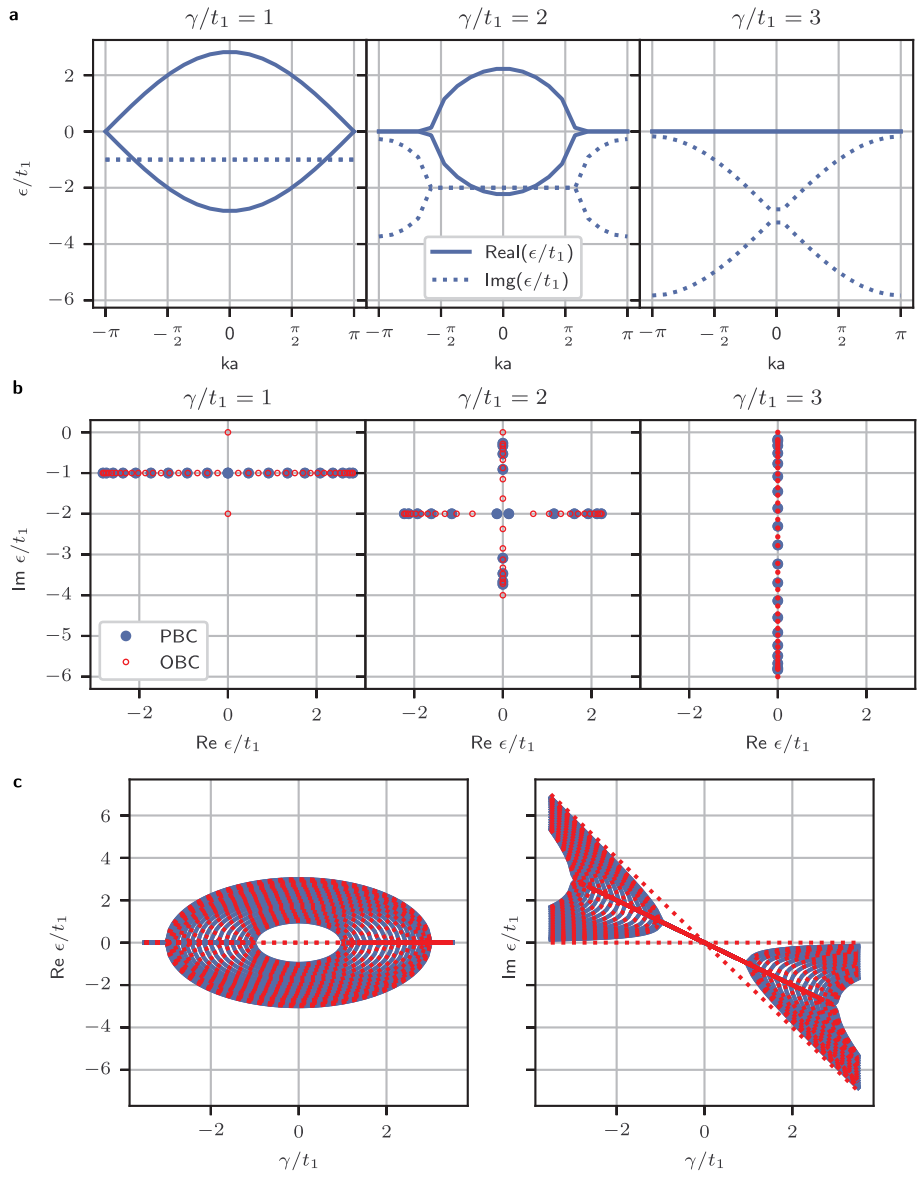

FIG. S6. Spectrum of the SSH model with alternating loss for PBC and OBC in the topological regime $t_2 = 2t_1$. A system size of 20 unit cells was used. **a**, As a function of ka for different values of γ. **b**, In the complex plane for different values of γ. The blue full circles results correspond to PBC, and the red empty circles to OBC. **c**, As a function of γ/t_1.

This system can once again be studied in the trivial and topological regime.

1. *Trivial Phase*

This system is clearly very similar to the system with alternating gain and loss, as can also be seen from Figs. S5a-c. Figs. S5a-b are just shifted down on the imaginary axis proportional to γ, while Fig. S5c shows how the spectrum depends on γ. Due to this imaginary offset, the system no longer has a $\mathcal{PT}$-symmetric phase, but rather presents passive $\mathcal{PT}$-symmetry. Similarly to the system with alternating gain and loss, the behaviour of the spectrum does not change much for different boundary conditions.

2. Topological Phase

Like in the trivial case, the spectrum is very similar to the alternating gain and loss Hamiltonian, but just shifted down on the imaginary axis, as can be seen in Figs. S6a-c. Again, there is no $\mathcal{PT}$-symmetric region due to the imaginary offset. The OBC case is discussed in detail in the main text.

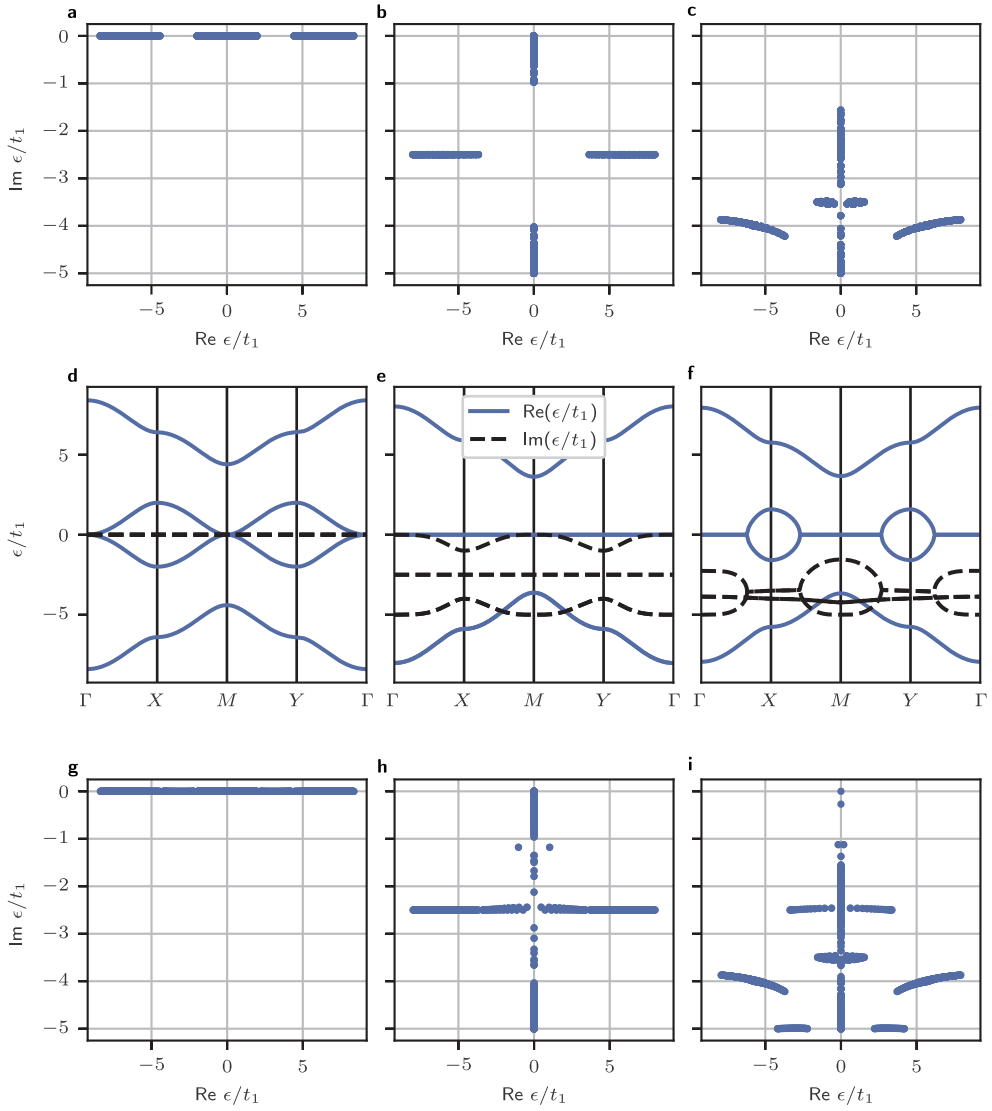

FIG. S7. Spectrum of the 2D SSH model, for $t_2/t_1 = 3.2$. **a - c**, The spectrum in the complex plane for PBC. **d - f**, Spectrum along the points of high symmetry for PBC. **g - i**, The spectrum in the complex plane for OBC. **a**, **d**, and **g** show the spectrum for the lossless 2D SSH model. **b**, **e**, and **h** show the spectrum for the system with loss along the diagonal of the unitcell (with $\gamma/t_1 = 5$), yielding a bimode: only two modes remain at zero energy. **c**, **f**, and **i** show the spectrum for the model with loss at three sites in the unit cell (with $\gamma/t_1 = 5$), yielding a monomode, as there is only one mode remaining at zero energy.

D. Alternating Loss 2D SSH

The SSH model can also be extended into two dimensions. This model has the same basic behaviour as the 1D SSH model, exhibiting three phases: $\mathcal{PT}$-symmetric phase, $\mathcal{PT}$-broken phase and a phase with an imaginary line gap. In Fig. S7 we show the spectrum of the 2D SSH model with no loss (Fig. S7a, d, and g) and with the loss distribution yielding a bimode (Fig. S7b, e, and h) and a monomode (Fig. S7c, f, and i). Especially Fig. S7c makes it very clear that all the bulk modes are destroyed in this loss configuration. For OBC, this would leave only one edge state.

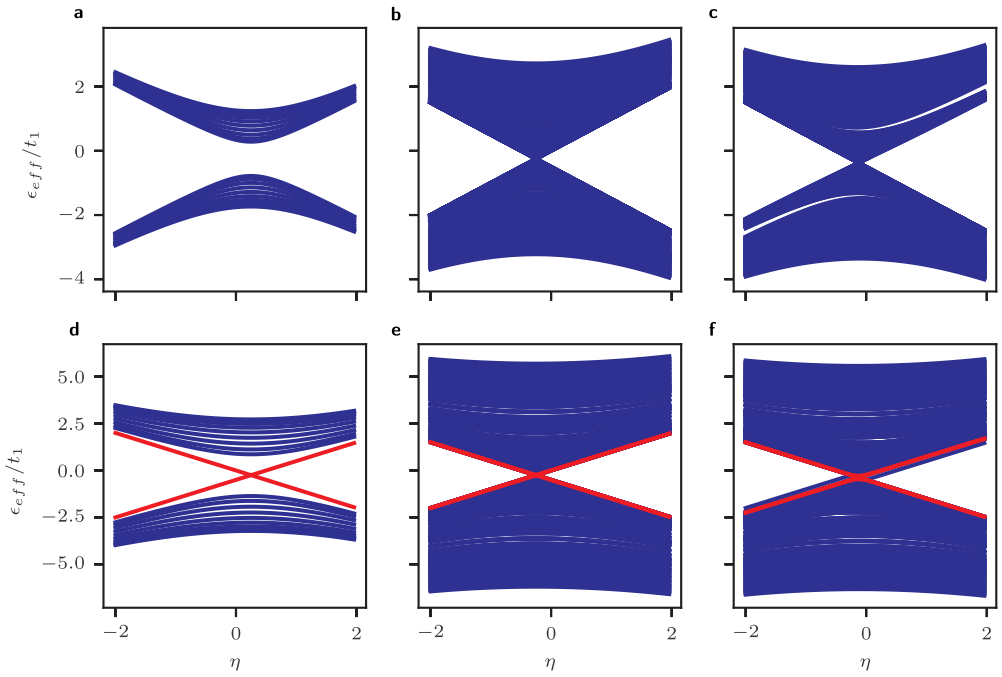

FIG. S8. Spectrum of the effective Hamiltonian for the 1D (**a** and **d**) and 2D SSH (**b**, **c**, **e**, and **f**) models. Spectrum in the trivial phase ($t_2/t_1 = 0.5$) in the **a** 1D SSH model, for the 2D SSH model with loss configuration **b** of Fig. 4b and **c** of Fig. 4c of the main text. Spectrum in the topological phase ($t_2/t_1 = 2$) shows linearly dispersing mode for both the **d** 1D SSH model and for the 2D SSH model with loss configuration **e** of Fig. 4b and **f** of Fig. 4c of the main text. Modes with an absolute value of the wavefunction larger than 0.8 at the edges (for 1D) and corners (for 2D) of the lattice are plotted in red; other modes are plotted in blue. We used 10 unit cells in each direction for this simulation.

II. EFFECTIVE HERMITIAN TOPOLOGICAL HAMILTONIAN

A. Chern Number for Alternating Loss 1D SSH

The Hermitian SSH model is described by the Bloch Hamiltonian*

$$H_{SSH}(k) = \begin{pmatrix} 0 & t_1 + t_2 e^{ik} \\ t_1 + t_2 e^{-ik} & 0 \end{pmatrix}. \tag{S13}$$

As a result of the block off-diagonal structure, it exhibits a sublattice symmetry (SLS) Γ, which takes the form

$$\Gamma H_{SSH}(k)\Gamma^{-1} = -H_{SSH}(k), \qquad \Gamma \equiv \begin{pmatrix} 1 & 0 \\ 0 & -1 \end{pmatrix}. \tag{S14}$$

Moreover, the SSH model displays both particle-hole symmetry (PHS) and time-reversal symmetry (TRS), such that it falls in the BDI symmetry class. It can be described by a $\mathbb{Z}$ invariant, which reduces, upon enforcing reflection symmetry, to a $\mathbb{Z}_2$ invariant. To obtain the monomode, we add an imaginary on-site potential to the model. However, such a term breaks SLS, as defined in Eq. (S14). This is indeed the case, but adding on-site loss, the Hamiltonian becomes non-Hermitian. For non-Hermitian Hamiltonians, chiral symmetry (CS) and sublattice symmetry are no longer the same:

$$\begin{aligned} \text{CS}: &\qquad \Gamma H(k)\Gamma^{-1} = -H^\dagger(k) \\ \text{SLS}: &\qquad \mathcal{S}H(k)\mathcal{S}^{-1} = -H(k). \end{aligned}$$

* Notice that, in this section, we used a different sign convention for the hopping. This, however, does not have any significant impact on the results.

It is straightforward to show that non-Hermitian CS is preserved if we have

$$H(k) = \begin{pmatrix} iP(k) & Q(k) \\ Q^\dagger(k) & iR(k) \end{pmatrix}, \qquad \Gamma = \begin{pmatrix} \mathbb{I} & 0 \\ 0 & -\mathbb{I} \end{pmatrix}, \tag{S15}$$

where $P(k)$ and $R(k)$ are Hermitian matrices and Q is non-Hermitian in general. Notice that the constraint that a chiral Hermitian Hamiltonian should be block off-diagonal is relaxed when considering non-Hermitian Hamiltonians. We consider the following non-Hermitian SSH model:

$$H_{NH-SSH}(k) = \begin{pmatrix} -i\gamma & t_1 + t_2 e^{ik} \\ t_1 + t_2 e^{-ik} & 0 \end{pmatrix}. \tag{S16}$$

Following Ref. [S3], we define an effective 2D Hermitian Hamiltonian

$$H^{\text{eff}}(k,\eta) = \Gamma\big(\eta\mathbb{I} - iH_{NH-SSH}(k)\big) = \begin{pmatrix} \eta - \gamma & -i\left(t_1 + t_2 e^{ik}\right) \\ i\left(t_1 + t_2 e^{-ik}\right) & -\eta \end{pmatrix}. \tag{S17}$$

We can associate a Chern number to this effective Hamiltonian, which is quantized as long as the Hamtiltonian is periodic in both k and η. While the Hamiltonian is periodic in the wave number k, the Hamiltonian is anti-periodic in η: $H^{\text{eff}}(k,\eta\to-\infty) = -H^{\text{eff}}(k,\eta\to\infty)$. To circumvent this problem, we perform the following, unitary transformation to obtain the compactified effective Hamiltonian

$$H^{\text{eff}}_{\text{cp}}(k,\eta) = \mathcal{R}_\eta H^{\text{eff}}(k,\eta)\mathcal{R}_\eta^\dagger, \tag{S18}$$

with

$$\mathcal{R}_\eta = \exp\left[i\frac{\pi}{4}(1+\tanh\eta)\mathcal{G}\right], \qquad \mathcal{G} = \begin{pmatrix} 0 & \mathbb{I} \\ \mathbb{I} & 0 \end{pmatrix}. \tag{S19}$$

Since we performed a unitary transformation, the spectra of $H^{\text{eff}}_{\text{cp}}(k,\eta)$ and $H^{\text{eff}}(k,\eta)$ are equivalent. The Chern number for $H^{\text{eff}}_{\text{cp}}(k,\eta)$ is now obtained through

$$C = \frac{1}{2\pi}\int_{-\infty}^{\infty} \mathrm{d}\eta \int_0^{2\pi} \mathrm{d}k\ \Omega_{k,\eta}, \tag{S20}$$

with the Berry curvature $\Omega_{k,\eta}$ given by

$$\Omega_{k,\eta} = 2\sum_{n\le n_F, m>n_F} \mathrm{Im}\,\frac{\left\langle \psi^n_{k,\eta}\right| \partial_k H^{\text{eff}}_{\text{cp}} \left|\psi^m_{k,\eta}\right\rangle \left\langle \psi^m_{k,\eta}\right| \partial_\eta H^{\text{eff}}_{\text{cp}} \left|\psi^n_{k,\eta}\right\rangle}{\left(E^{(n)}_{k,\eta} - E^{(m)}_{k,\eta}\right)^2}. \tag{S21}$$

Here, $E^{(i)}_{k,\eta}$ and $\left|\psi^i_{k,\eta}\right\rangle$ are the eigenvalues and eigenstates of the i-th band of $H^{\text{eff}}_{\text{cp}}$, and n_F is the number of occupied bands. For $H^{\text{eff}}_{\text{cp}}$ corresponding to the non-Hermitian SSH model, the eigenvalues are given by

$$E^{\pm}_{k,\eta} = \gamma \pm \sqrt{t_1^2 + t_2^2 + \eta^2 + 2t_1 t_2 \cos k}, \tag{S22}$$

while the eigenvectors are given by

$$\left|\psi^{\pm}_{k,\eta}\right\rangle = \begin{pmatrix} i\frac{\sqrt{t_1^2+t_2^2+\eta^2+2t_1t_2\cos k} \mp (t_1+t_2\cos k)\cos\left(\frac{\pi}{2}\tanh\eta\right) + \eta\sin\left(\frac{\pi}{2}\tanh\eta\right)}{\mp\eta\cos\left(\frac{\pi}{2}\tanh\eta\right) + it_2\sin k + (t_1+t_2\cos k)\sin\left(\frac{\pi}{2}\tanh\eta\right)} \\ 1 \end{pmatrix}. \tag{S23}$$

From the expression of the Berry curvature, we observe that it is independent of γ. Moreover, we obtain

$$C = \begin{cases} 0 & |t_1| > |t_2| \\ 1 & |t_1| < |t_2| \end{cases}, \tag{S24}$$

which reveals the topological phase for the (non-Hermitian) SSH model. Edge modes of the 1D SSH model appear as linearly dispersing modes of the effective Hamiltonian [S3], as shown in Figs. S8a and d, as expected for the edge states of a Chern insulator.

B. Topological Defect

We now use the Jackiw-Rebbi [S4, S5] construction to obtain the localization at the topological defect. Writing the effective Hamiltonian (S17) in terms of Pauli matrices σ_i,

$$H^{\text{eff}}(k,\eta) = \left(\eta - \frac{\gamma}{2}\right)\sigma_z - \frac{\gamma}{2}\mathbb{I} + \left[t_1 + t_2\cos(k)\right]\sigma_y + t_2\sin(k)\sigma_x, \tag{S25}$$

we see that the gap closing occurs for $t_1 = t_2$, $k = \pm\pi$ and $\eta = \gamma/2$. Close to the phase transition and in the vicinity of the gap closing point, we can do a low-energy description of this model[†]

$$H^{\text{eff}}(p,\eta) = \left(\eta - \frac{\gamma}{2}\right)\sigma_z + t_2 M\sigma_y - t_2 p\sigma_x + \mathcal{O}(p^2), \tag{S26}$$

where $p = k - \pi$, the mass term $M = (t_1 - t_2)/t_2$, and we changed the energy reference to neglect the term proportional to the identity. Notice that the gap closing then occurs for $p = 0$ and $M = 0$, and the sign of the mass term determines whether the system is trivial ($M > 0$) or topological ($M < 0$). Associated with this low-energy model, there is a continuum model

$$H^{\text{eff}}(x,\eta) = \left(\eta - \frac{\gamma}{2}\right)\sigma_z + t_2 M\sigma_y + it_2\partial_x\sigma_x, \tag{S27}$$

since the momentum is the derivative $p = -i\partial_x$ along the coordinate x of the lattice.

Using the continuum Hamiltonian, a change in the hopping parameters along the lattice is translated into a spatially dependent mass term $M(x)$. A topological defect is a domain wall between a topological ($M < 0$) and a trivial ($M > 0$) lattice, so we can model it by a profile of mass that changes sign across the boundary and vanishes at the defect. Therefore, for at least one value of η, there will be a localized zero-energy solution of the Hamiltonian

$$H^{\text{eff}}(x,\eta = -\gamma/2)\Psi_{DW}(x) = \left[t_2 M(x)\sigma_y + it_2\partial_x\sigma_x\right]\Psi_{DW}(x) = 0 = \left[M(x)\mathbb{I} + \partial_x\sigma_z\right]\Psi_{DW}(x). \tag{S28}$$

Notice that we multiplied the matrix applied on $\Psi_{DW}(x)$ by σ_y and divided by t_2 to obtain the last equality.

Writing now $\Psi_{DW}(x)$ in terms of eigenstates of σ_z, $\chi^+ = \begin{pmatrix}1 & 0\end{pmatrix}^T$ and $\chi^- = \begin{pmatrix}0 & 1\end{pmatrix}^T$,

$$\Psi_{DW}(x) = \sum_{\sigma=\pm1} c_\sigma \psi^\sigma_{DW}(x)\chi^\sigma, \quad \sum_\sigma |c_\sigma|^2 = 1, \quad \int_{-\infty}^{\infty} dx\, |\psi^\sigma_{DW}(x)|^2 = 1, \tag{S29}$$

we can obtain a differential equation for $\psi^\sigma_{DW}(x)$ in terms of the eigenvalues σ of σ_z,

$$\left[M(x) + \sigma\partial_x\right]\psi^\sigma_{DW}(x) = 0 \Rightarrow \psi^\sigma_{DW}(x) = \mathcal{N}e^{-\sigma\int_{-\infty}^{x} M(x')dx'}, \tag{S30}$$

where $\mathcal{N}$ is a normalization factor.

For a system with the topological phase on the left and the trivial phase on the right of the domain wall, we obtain localized solutions just for $\sigma = 1$; therefore, $c_- = 0$ and $c_+ = 1$. Notice that at the domain wall, the Hamiltonian as a function of η is given by

$$H^{\text{DW}}(\eta) = \langle\Psi_{DW}|H^{\text{eff}}|\Psi_{DW}\rangle = \eta - \frac{\gamma}{2}, \tag{S31}$$

which exhibits a linear dispersion. Moreover, there is a localized solution only at the boundary between the trivial ($M > 0$) and topological ($M < 0$) phases, which characterizes this defect as a topological defect.

C. Effective Hamiltonian for the 2D SSH

The lossy 2D SSH model also has a Bloch Hamiltonian with non-Hermitian CS, cf (S15),

$$H_{\text{NH-2d-SSH}}(k_x,k_y) = \begin{pmatrix} iP & Q(k_x,k_y) \\ Q^\dagger(k_x,k_y) & iR \end{pmatrix} \tag{S32}$$

[†] The quadratic term can be added to fix the boundary conditions.

with $Q(k) = [t_1 + t_2\cos(k_x)]\,\mathbb{I} + it_2\sin(k_x)\sigma_z + [t_1 + t_2\cos(k_y)]\,\sigma_x - t_2\sin(k_y)\sigma_y$ using the choice of basis from Ref. [S6]. $R = -\gamma\mathbb{I}$, $P = 0$ and $R = -\gamma\mathbb{I}$, $P = -\gamma\,(\mathbb{I} + \sigma_z)\,/2$ for the loss configuration of Fig. 4b and Fig. 4c, respectively, of the main text.

We see that we can extend the method of Ref. [S3] to define an effective Hermitian Hamiltonian by adding a third dimension to the problem

$$\begin{aligned} H^{\text{eff}}(k_x, k_y, \eta) &= \Gamma\left[\eta\mathbb{I} - iH_{\text{NH-2D-SSH}}(k_x, k_y)\right] \\ &= H_d(\eta) + [t_1 + t_2\cos(k_x)]\sigma_y \otimes \mathbb{I} + t_2\sin(k_x)\sigma_x \otimes \sigma_z + [t_1 + t_2\cos(k_y)]\sigma_y \otimes \sigma_x - t_2\sin(k_y)\sigma_y \otimes \sigma_y, \end{aligned} \tag{S33}$$

where $\Gamma = \sigma_z \otimes \mathbb{I}$ and the diagonal H_d part of the Hamiltonian is given by, $H_d = -\gamma/2\,\mathbb{I} \otimes \mathbb{I} + (\eta - \gamma/2)\,\sigma_z \otimes \mathbb{I}$ and $H_d = -3\gamma/4\,\mathbb{I} \otimes \mathbb{I} + (\eta + \gamma/4)\,\sigma_z \otimes \mathbb{I} - \gamma/4\,\mathbb{I} \otimes \sigma_z - \gamma/4\,\sigma_z \otimes \sigma_z$ for the loss configuration in Fig. 4b and Fig. 4c of the main text, respectively. We show the dispersion relation of both cases in Fig. S8. The corner modes of the 2D non-Hermitian model appear as linearly dispersing modes for the effective Hamiltonian, although they are not the only ones with this property because the bulk of this system is not gapped.

D. Corner States of the Lossy 2D SSH Model

The Jackiw-Rebbi construction can be generalized to describe corner states in higher-order topological phases [S7, S8] by considering a corner as an x-domain wall in the y-edge and vice-versa, and ensuring the compatibility of the two solutions. To use the continuum Hamiltonian with a position-dependent mass term, we consider that t_1 can be different along x and y. We see then that the gap closing is given by $H_D = 0$, $t_1^x = t_1^y = t_2$, and $k_x = k_y = \pi$. Therefore, we again obtain a low-energy continuum theory

$$H^{\text{eff}}(p_x, p_y, \eta) = H_d(\eta) + t_2 M^x \sigma_y \otimes \mathbb{I} - t_2 p_x \sigma_x \otimes \sigma_z + t_2 M^y \sigma_y \otimes \sigma_x + t_2 p_y \sigma_y \otimes \sigma_y, \tag{S34}$$

where $M^{x/y} \equiv \left(t_1^{x/y} - t_2\right)/t_2$. The higher-order topological phase is characterized by having both M^x and M^y negative, while the trivial phase has both positive. An edge of the HOT phase reproduces a domain wall between the HOT phase and the vacuum (which is trivial). To show that these states are topological, we focus on the upper right corner, which we locate at $x = y = 0$, but the entire discussion is easily extended to the other three corners.

A zero-energy mode in the right x-edge should satisfy

$$(t_2 M^x(x)\sigma_y \otimes \mathbb{I} + it_2\partial_x\sigma_x \otimes \sigma_z)\,\Psi^{x-\text{edge}}(x) = 0 = (M^x(x)\mathbb{I} \otimes \mathbb{I} + \partial_x\sigma_z \otimes \sigma_z)\,\Psi^{x-\text{edge}}(x). \tag{S35}$$

Writing $\Psi^{x-\text{edge}}(x)$ in terms of the eigenstates $\chi^{\sigma,\sigma'}$ of $\sigma_z \otimes \sigma_z$

$$\Psi^{x-\text{edge}}(x) = \sum_{\sigma,\sigma'=\pm1} c_{\sigma,\sigma'}\psi^{\sigma,\sigma'}_{x-\text{edge}}(x)\chi^{\sigma,\sigma'}, \quad \sum_{\sigma,\sigma'} |c_{\sigma,\sigma'}|^2 = 1, \quad \int_{-\infty}^{\infty} dx\,\left|\psi^{\sigma}_{x-\text{edge}}(x)\right|^2 = 1, \tag{S36}$$

$$\chi^{+,+} = \begin{pmatrix}1\\0\\0\\0\end{pmatrix}, \quad \chi^{+,-} = \begin{pmatrix}0\\1\\0\\0\end{pmatrix}, \quad \chi^{-,+} = \begin{pmatrix}0\\0\\1\\0\end{pmatrix}, \quad \chi^{-,-} = \begin{pmatrix}0\\0\\0\\1\end{pmatrix}, \tag{S37}$$

and using that the eigenvalues of $\sigma_z \otimes \sigma_z$ are $\sigma\sigma'$, we obtain the equation for $\psi_{x-\text{edge}}$

$$(M^x(x) + \sigma\sigma'\partial_x)\,\psi^{x-\text{edge}}(x) = 0 \Rightarrow \psi^{x-\text{edge}}(x) = \mathcal{N}^x e^{-\sigma\sigma'\int_{-\infty}^{x} M^x(x')dx'}. \tag{S38}$$

Setting the edge at $x = 0$, we have a mass profile that has a negative (positive) value for negative (positive) x. Therefore, the solutions localized in the edge are given by $\sigma\sigma' = 1$, which is satisfied by $\sigma = \sigma' = \pm1$. For convenience, we use the subscript $+$ $(-)$ in the first (second) solution. The components of the x-surface Hamiltonian are given by

$$\begin{aligned} [H^{x-\text{surface}}(p_y)]_{l,m} &= \chi^{l\dagger}\left[t_2 M^y \sigma_y \otimes \sigma_x + t_2 p_y \sigma_y \otimes \sigma_y\right]\chi^m \\ &= t_2 M^y(\sigma_y)_{lm} + t_2 p_y(\sigma_x)_{lm}. \end{aligned} \tag{S39}$$

Considering now the corner as being a (y) domain wall for this surface Hamiltonian, we look for a solution $\Psi^{\text{corner}}(y)$ which satisfies

$$(t_2 M^y \sigma_y - it_2\partial_y\sigma_x)\,\Psi^{\text{corner}}(y) = 0 = (M^y\mathbb{I} - \partial_y\sigma_z)\,\Psi^{\text{corner}}(y). \tag{S40}$$

In terms of the spinors of the first solutions

$$\Psi^{\text{corner}}(y) = \sum_{\tau=\pm1} c_\tau \psi^\tau_{\text{corner}}(y)\chi^\tau, \tag{S41}$$

we obtain

$$\left(M^y(y) - \tau\partial_y\right)\psi^\tau_{\text{corner}}(y) = 0 \rightarrow \psi^\tau_{\text{corner}}(y) = \mathcal{N}^y e^{\tau \int_{-\infty}^{y} M^y(y')dy'}. \tag{S42}$$

Therefore, we see that the localized solution is the one with $\tau = -1$, which corresponds to χ^-. Accordingly, the wavefunction for the corner state is given by

$$\Psi^{\text{corner}}(x,y,\eta) = \mathcal{N}^x\mathcal{N}^y e^{-\int_{-\infty}^{x} M^x(x')dx'} e^{-\int_{-\infty}^{y} M^y(y')dy'} \psi(\eta) \begin{pmatrix}0\\0\\0\\1\end{pmatrix}. \tag{S43}$$

We have then the corner Hamiltonian

$$H^{\text{corner}}(\eta) = \langle\Psi^{\text{corner}}|H^{\text{eff}}|\Psi^{\text{corner}}\rangle = \chi^{+\dagger}H_d(\eta)\chi^+ = -\eta + \gamma \tag{S44}$$

for both loss configurations. The same construction can be used to obtain the other corner modes, the only difference being how $M^{x/y}$ changes across the boundaries, which affects both the spatial and spinorial forms of the corner states.

III. EXPERIMENTAL DETAILS

In this study, we present observations of topological models in waveguide structures. To achieve this, a coherent light beam from a tunable laser (Cameleon Ultra II, Coherent) was launched into a glass sample using a 100× objective with a numerical aperture (NA) of 0.9. This configuration allows for individual excitation of each waveguide composing the structure. The output light of the glass sample was collected using a 20× objective, and the image profile of each individual waveguide forming the topological structure was captured using a CCD camera.

The topological photonic 3D waveguide lattice structures (2D spatial, 1D time) were fabricated using a pulsed femtosecond (fs) laser (BlueCut fs laser from Menlo Systems). The fs laser produced light pulses centered at a wavelength of 1030 nm, with a duration of 350fs, and a repetition rate of 1 MHz. The waveguides were written in a Corning EAGLE2000 alumino-borosilicate glass sample with dimensions of $L = 50, W = 25$, and $h = 1.1$ mm.

To inscribe the waveguide structures, pulses of 210 nJ were focused using a 50X objective of 0.55 NA. The waveguides were written at depths between 70 to 175μm under the surface, according to the designed structure, while the sample was translated at a constant speed of 30 mm/s by a high-precision three-axis translation stage (A3200, Aerotech Inc.). The fabricated waveguides supported a Gaussian single mode at 780 nm, with a mode field diameter $\left(1/e^2\right)$ of approximately $6 - 8\mu$m. The mechanism of ultrafast laser pulses-material interaction gave a refractive index increase of about 2×10^{-4}. The propagation losses were estimated to be around 0.3 dB/cm, and the birefringence was in the order of 7×10^{-5}.

IV. NUMERICAL PREDICTIONS

Fig. S9 shows the experimental results (first column) alongside the theoretical predictions for the 1D SSH experiments (second column). These are the same numerical results as represented in Fig. 3 by circles, but here they are shown on a similar color scale to the experiments. Fig. S10 displays the time-evolution of the inserted light for the simple tight-binding case (Fig. S10a), and the trivial SSH case (Fig. S10b). Due to the paraxial equation, we can relate the length of the waveguides to time. As light moves along the waveguide, time can be promptly determined by the length divided by the speed of light. Therefore, this spatial direction actually corresponds to a time direction. The T_{exp} can be calculated by scaling the length of the waveguide by the hopping parameter t_1, yielding $T_{exp} = Lt_1$. This makes it clear that the theoretical predictions for these two models rely heavily on the duration of the experiment (length of the waveguide). Fig. S11 shows the theoretical results for the 2D SSH model. Here, a larger system size was used than in the experiment. However, the same behaviour can be seen, with the realization of a bimode and a monomode.

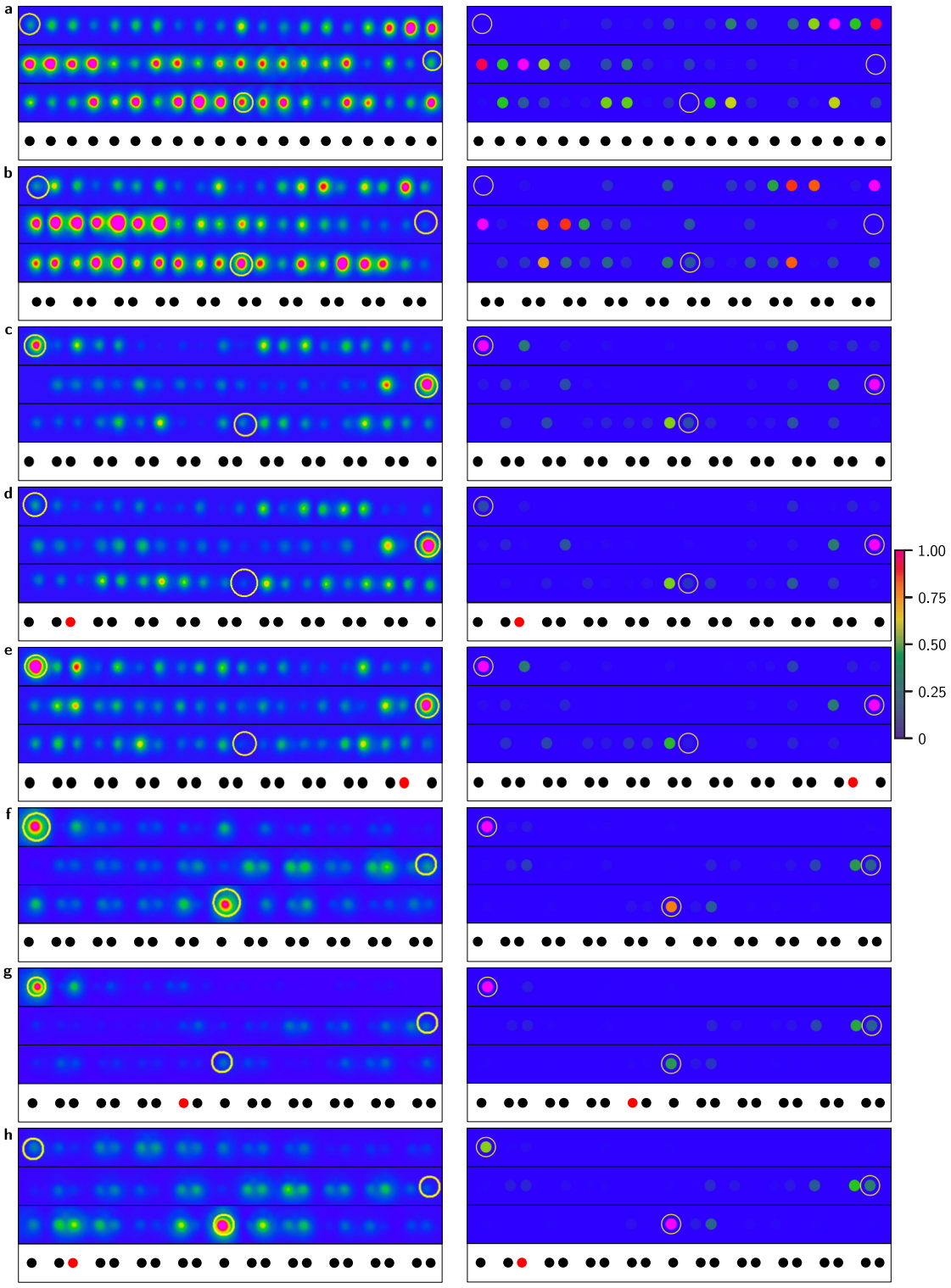

FIG. S9. Numerical results of Fig. 3, alongside the experimental data. The left column gives the experimental data, which can also be seen in the main text. The right column shows the numerical results. Yellow circles signal the point at which light was injected. **a**, Tight-binding chain (black dots) with $t_1 = t_2$ dispersing into the bulk. **b**, Trivial SSH chain with $t_1/t_2 = 2$ dispersing into the bulk. **c**, Topological SSH chain without loss with $t_2/t_1 = 2$. Localised edge modes can be clearly observed. **d**, When we add loss ($\gamma/t_1 = 0.5$) at the red-dot site near the left edge, one of the edge modes disappears, revealing the monomode. **e**, This is not the case when the loss is applied far away from the left edge. In this case, the edge mode does not decay within the experimental time scale. **f**, A topological defect is added to the system ($t_2/t_1 = 3.2$). Now, there is a left edge mode, as well as a mode pinned on the defect. **g**, Loss is placed on the red-dot site near the defect. This destroys the mode at the defect, but leaves the monomode. **h**, By placing the loss on the red-dot site near the left edge, the edge mode gets destroyed, but not the defect mode.

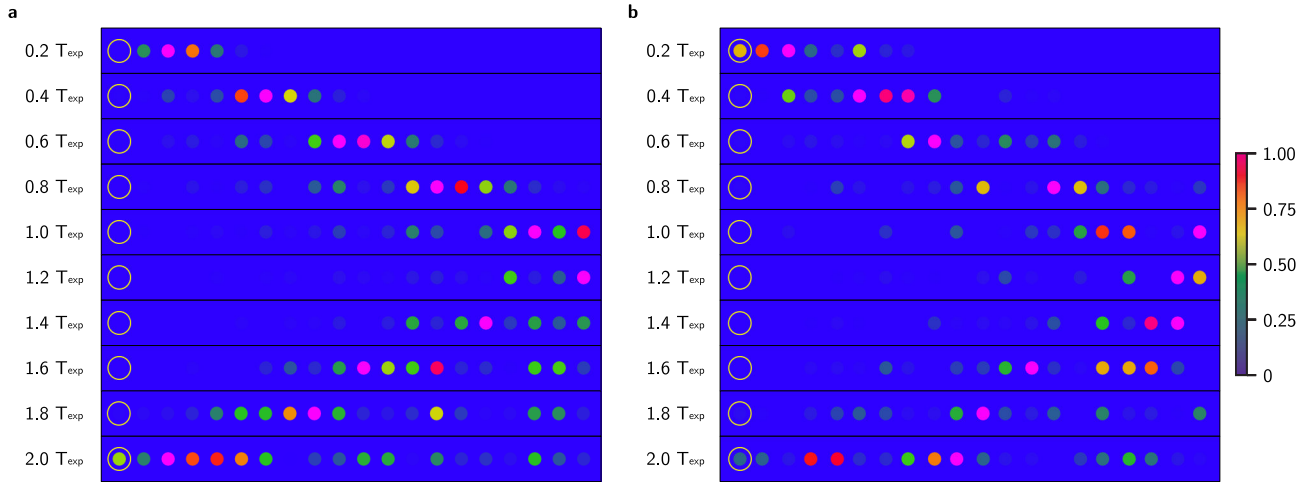

FIG. S10. Numerical predictions of the time propagation of Figs. 3a-b. **a**, Time propagation of the tight-binding chain. Clearly, a wave is propagating from its insertion point on the left, to the right. At around the time of the experiments, the wave hits the right edge of the chain and reflects back. **b**, Time propagation of the trivial SSH chain. We see a similar behaviour as for **a**.

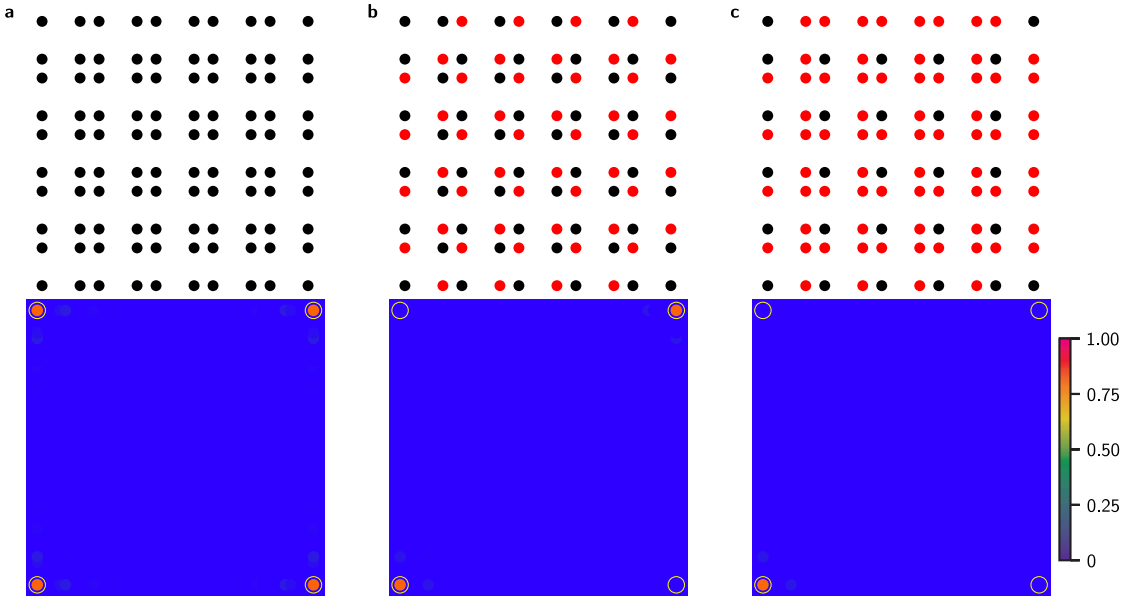

FIG. S11. Numerical prediction of the bi- and monomodes in the 2D SSH model for 10x10 unit cells with $t_2/t_1 = 3.2$ and $\gamma/t_1 = 5$. Yellow circles indicate the point at which light was injected. The top row shows the loss locations in the lattice (red dots) and the bottom row the predictions, for injecting into the four corners. **a**, No loss, showing four distinct corner modes. **b**, Loss on two sublattices. This breaks the C_{4v} symmetry of the system into C_{2v} and leads to bimodes. **c**, By adding loss on three sublattices, the C_{2v} symmetry is broken and the monomode emerges.

V. ADDITIONAL EXPERIMETAL DATA

Figs. S12 and S13 show the full experimental data of the 1D chain experiments, obtained upon inserting light in each waveguide.

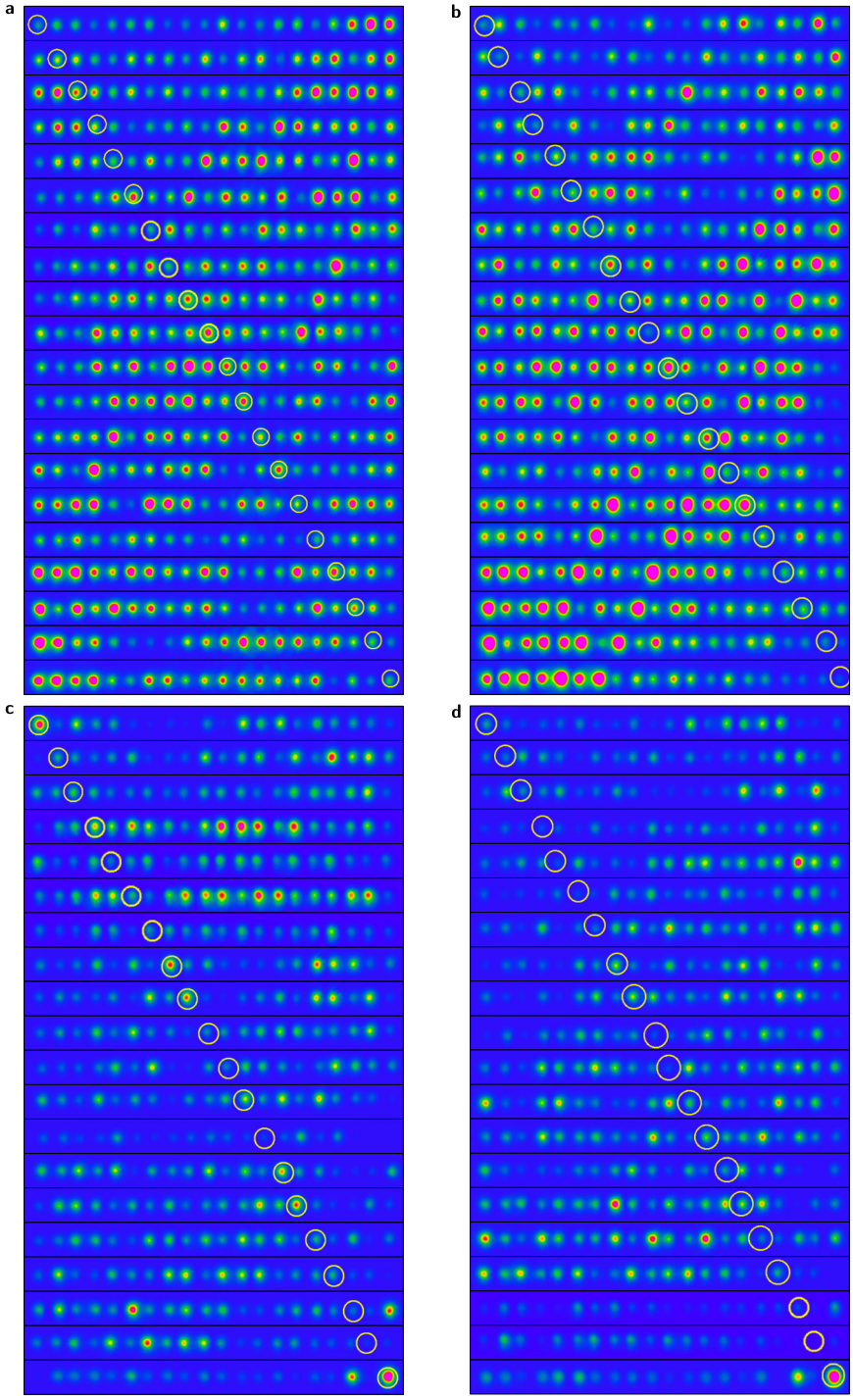

FIG. S12. Experimental results for all insertion points. **a**, Results of the tight-binding chain with no loss, from Fig. 3a. **b**, Results of the topologically trivial chain with no loss, from Fig. 3b. **c**, Results of the topological chain with no loss, from Fig. 3c. **d**, Results of the topological chain with loss, from Fig. 3d.

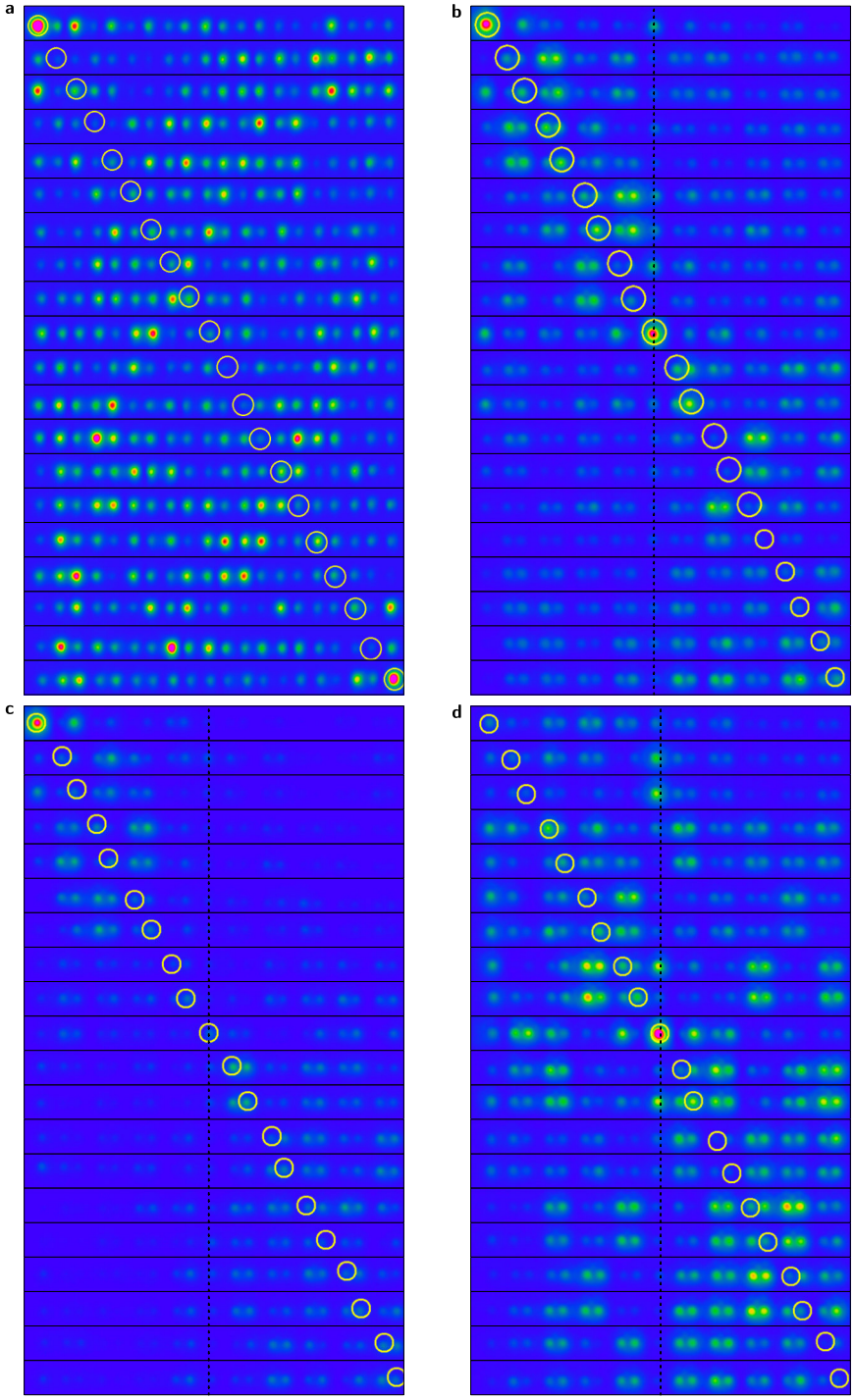

FIG. S13. Experimental results for all insertion points. **a**, Results of the topological chain with loss on the "wrong" (far away) side of the lattice, from Fig. 3e. **b**, Results of the topological defect chain with no loss, from Fig. 3f. The position of the topological defect is indicated by a dotted line. **c**, Results of the topological defect chain with loss engineered in a way to destroy the defect mode, from Fig. 3g. **d**, Results of the topological defect chain with loss designed to destroy the left edge mode, from Fig. 3h.

REFERENCES

[S1] F. Roccati, G. M. Palma, F. Ciccarello, and F. Bagarello, Non-Hermitian Physics and Master Equations, OSID **29**, 2250004 (2022).

[S2] M.-A. Miri and A. Alù, Exceptional points in optics and photonics, Science **363**, eaar7709 (2019).

[S3] W. Brzezicki and T. Hyart, Hidden Chern number in one-dimensional non-Hermitian chiral-symmetric systems, Phys. Rev. B **100**, 161105 (2019).

[S4] R. Jackiw and C. Rebbi, Solitons with fermion number $\frac{1}{2}$, Phys. Rev. D **13**, 3398 (1976).

[S5] R. Arouca, A. Cappelli, and H. Hansson, Quantum Field Theory Anomalies in Condensed Matter Physics, SciPost Phys. Lect. Notes , 62 (2022).

[S6] W. A. Benalcazar and A. Cerjan, Bound states in the continuum of higher-order topological insulators, Phys. Rev. B **101**, 161116 (2020).

[S7] W. A. Benalcazar, B. A. Bernevig, and T. L. Hughes, Electric multipole moments, topological multipole moment pumping, and chiral hinge states in crystalline insulators, Phys. Rev. B **96**, 245115 (2017).

[S8] A. K. Ghosh, T. Nag, and A. Saha, Floquet generation of a second-order topological superconductor, Phys. Rev. B **103**, 045424 (2021).